The Planetary Science Journal, 3:224 (23pp), 2022 September https://doi.org/10.3847/PSJ/ac88c2

Surface Conditions and Resource Accessibility at Potential Artemis Landing Sites 007 and 011

Nandita Kumari[1], Jordan M. Bretzfelder[2], Indujaa Ganesh[3,4], Antonio Lang[5], and David A. Kring[6]
[1] Department of Geosciences, Stony Brook University, Stony Brook, NY, USA; Nandita.kumari@stonybrook.edu
[2] Department of Earth, Planetary, and Space Sciences, University of California, Los Angeles, Los Angeles, CA, USA; jbretzfelder@g.ucla.edu
[3] Department of Planetary Sciences, University of Arizona, Tucson, AZ, USA; iganesh@alaska.edu
[4] Geophysical Institute, University of Alaska Fairbanks, Fairbanks, AK, USA
[5] University at Buffalo, Albany, NY, USA; anlang@buffalo.edu
[6] Center for Lunar Science and Exploration, Lunar and Planetary Institute, Houston, TX, USA; Kring@lpi.usra.edu
Received 2022 May 5; revised 2022 August 2; accepted 2022 August 4; published 2022 September 28

Abstract

International efforts are underway to explore the Moon's south polar region with robotic and human missions. These missions will address key scientific and exploration objectives in a region rich with possibilities, designed to develop a sustained lunar presence. To assist a trade study among six potential landing sites identified for Artemis astronauts, we examined two of those sites: 007 and 011. We find that (1) many craters in the vicinity of Site 007 excavated and expose ejecta from Shackleton and Slater; additionally, numerous craters around Site 011 expose Cabeus and de Gerlache ejecta; (2) dense boulder fields occur near a large permanently shadowed region (PSR) at Site 007 and near the point of highest surface illumination in Site 011, which may affect landing and surface exploration activities; (3) despite some surface roughness, both sites 007 and 011 are traversable and contain exploration targets suitable for in situ resource utilization; (4) sites 007 and 011 receive higher average illumination than previously reported for sites 001 and 004; and (5) PSRs, seasonally shadowed regions, and cold traps at both sites offer opportunities to sample volatiles.

Unified Astronomy Thesaurus concepts: Selenology (1441); Lunar surface (974)

1. Introduction

The polar regions of the Moon are attracting the attention of lunar explorers because of two resources that may sustain those exploration efforts: solar power and ice. In the polar regions, the Sun circumnavigates the pole near the horizon rather than passing overhead. Thus, the potential exists for topographically high features to be illuminated by sunlight for greater than 50% of the time, rather than 14 days of sunlight, followed by 14 days of darkness, as experienced at the Apollo landing sites. A series of studies using Clementine images (Bussey et al. 1999), Kaguya (SELENE) laser altimeter data (Kato et al. 2008; Noda et al. 2008), Lunar Orbiter Laser Altimeter (LOLA) topography data (Mazarico et al. 2011; Glaser et al. 2014), and Lunar Reconnaissance Orbiter Camera (LROC) images (Speyerer & Robinson 2013) revealed several sites where illumination may exceed 80% (Bussey et al. 2010; Mazarico et al. 2011). If solar power at those sites can be used in situ, and/or transmitted or transported to other locations where surface operations are needed, then solar power could sustain surface activity. Six sites were identified because of their potential to host volatiles, higher solar illumination, direct-to-Earth communication, and less challenging terrain for rovers and astronauts. These were given numerical designations as potential Artemis landing sites and include sites 001, 004, 007, 011, 102, and 105 (NASA 2020).

The topography in the south polar region of the Moon is dramatic, with massif summits rising ∼2300 m above the lunar datum and the floors of impact craters falling ∼4300 m below the lunar datum. The extreme topography in an area where sunlight originates from only a few degrees above the horizon casts long shadows and, in some cases, creates permanently shadowed regions (PSRs). Temperatures in PSRs may be only a few degrees above absolute zero. The Diviner instrument has recorded temperatures as low as 30 K (Paige et al. 2010) in the polar regions. It has long been recognized that such cold temperatures in the polar regions can trap volatile materials like water as ice (Watson et al. 1961; Arnold 1976; Ingersoll et al. 1992; Feldman et al. 1998). Volatile constituents from the solar wind (e.g., Crider & Vondrak 2000), micrometeorite impacts (Benna et al. 2019), larger, sporadic impact events and, in an earlier epoch of lunar history, the basin-forming impacts (Arnold 1979), crustal leaking (Schorghofer & Taylor 2007), and volcanic eruptions (Kring et al. 2014; Needham & Kring 2017; Kring et al. 2021) may have contributed to the ices detected in these PSRs. Such volatile material, if present in abundance, could be harvested for crew consumables, radiation shielding, and propellants (Kring et al. 2020e, 2020f). The colocation of these potential ice deposits with points of illumination is a principal driver for polar exploration.

Ice has been inferred based on a combination of radar anomalies and neutron flux anomalies (Nozette et al. 2001; Thomson et al. 2012). Enhanced hydrogen abundances were detected using neutron data (Elphic et al. 2007; Teodoro et al. 2010; Miller et al. 2014; Lawrence et al. 2015), higher off-band albedos in the poles (Gladstone et al. 2012), and high reflectance at 1064 nm using LOLA data (Lucey et al. 2014). Water ice and other volatiles were detected in material entrained in a plume excavated by the Lunar Crater Observation and Sensing Satellite spacecraft following its impact with the floor of the Cabeus crater (Colaprete et al. 2010). Water ice exposed on the surface was detected in Moon Mineralogy

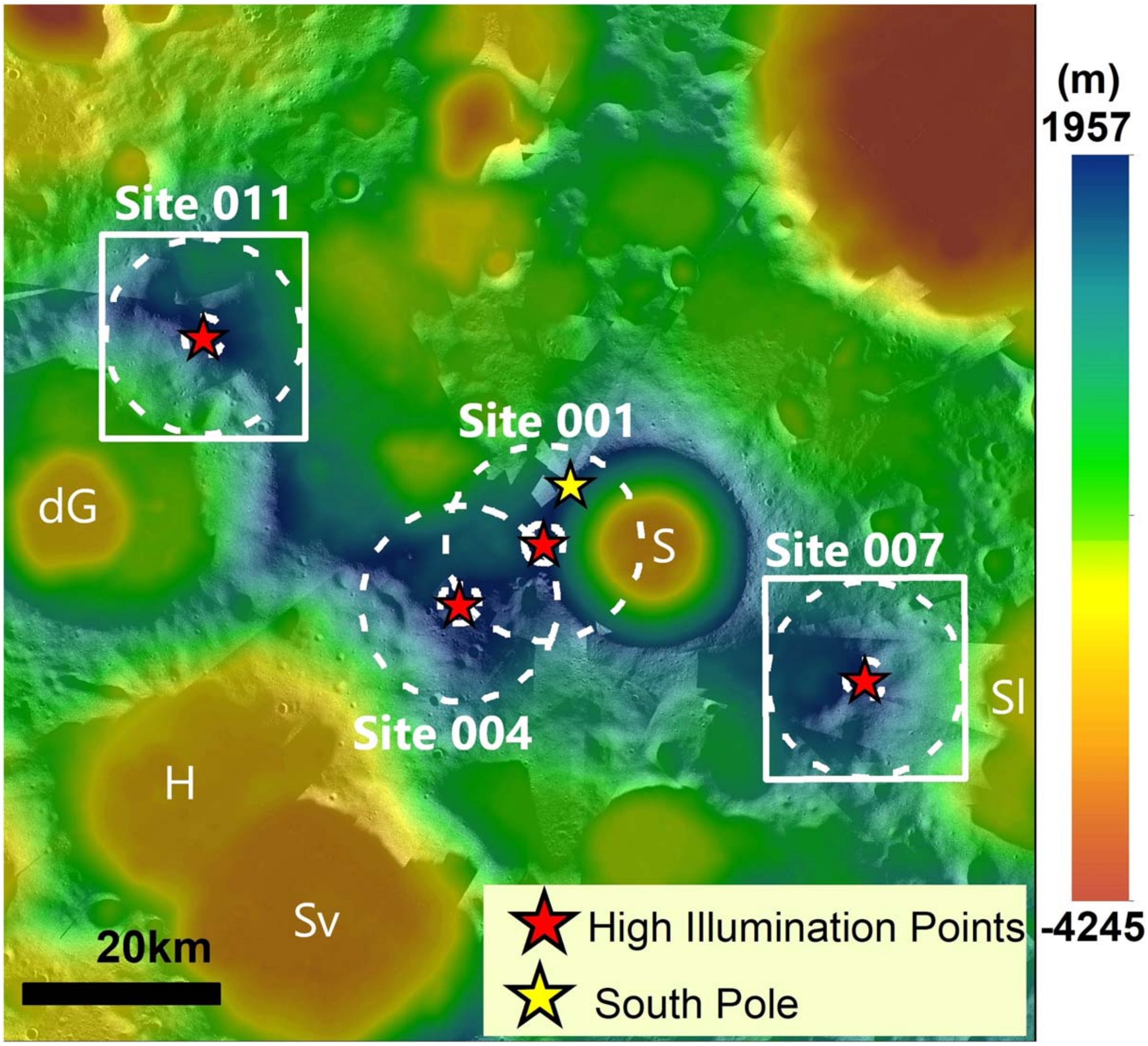

Figure 1. LOLA digital elevation model (20 m px^{-1}) overlaid on a LRO-NAC mosaic with the south pole (yellow star) and proposed landing sites identified in a NASA (2020) report (red stars), which are coincident with the points of highest illumination from Mazarico et al. (2011) marked. The "S" indicates the Shackleton crater, "Sl" indicates the Slater crater, "dG" indicates the de Gerlache crater, "H" indicates the Henson crater, and "Sv" indicates the Sverdup crater.

Mapper (M3) spectra throughout the south polar region (Li et al. 2018). However, other studies based on radar (Campbell et al. 2006), topography (Haruyama et al. 2008, 2013), and laser reflectance observations (Zuber et al. 2012) do not support the presence of water ice on the surface. The nature of M3 measurements being spectroscopic make it difficult to differentiate if it is from a mineral with OH molecules in its structure or ice crystals. This motivates the need for lunar surface exploration by robotic assets (e.g., the Volatiles Investigating Polar Exploration Rover, VIPER) and crewed missions (e.g., Artemis) to ground-truth these potential detections.

The need to characterize the geology and quantify resource abundances on the lunar surface have prompted several previous studies of landing sites in the south polar region (Lemelin et al. 2014; Heldmann et al. 2015; Speyerer et al. 2016; Allender et al. 2019; Kring et al. 2020a,2020b, 2020c, 2020d, 2020e, 2020f, 2020g, 2020h; Lemelin et al. 2021).

In the study reported here, two of proposed Artemis landing sites (NASA 2020) are examined: Site 007 between Shackleton and Slater craters and Site 011 on the rim of de Gerlache crater (Figure 1). These two locations were identified as potential landing sites because they are illuminated ~80% of the time (NASA 2020). They are within the 15 × 15 km regions that are candidates for the Artemis III mission (NASA 2022): Peak Near Shackleton (around site 007) and de Garlache Rim 1 (around site 011). We further evaluate that illumination, the accessibility of nearby PSRs, and the geologic context of the sites to determine their suitability to address a broader range of scientific objectives (National Research Council of the National Academies 2007).

In the analyses that follow, we consider two different sizes of exploration zones (EZs): a 2 km radial area suitable for a mission limited by walking extravehicular activity (EVA) and a 10 km radial area suitable for a mission with an unpressurized rover (e.g., Lunar Terrain Vehicle).

2. Geological Context

The topography and composition of the lunar south polar terrain has largely been shaped by the 2500 km diameter pre-Nectarian South Pole–Aitken (SPA), basin which produced a

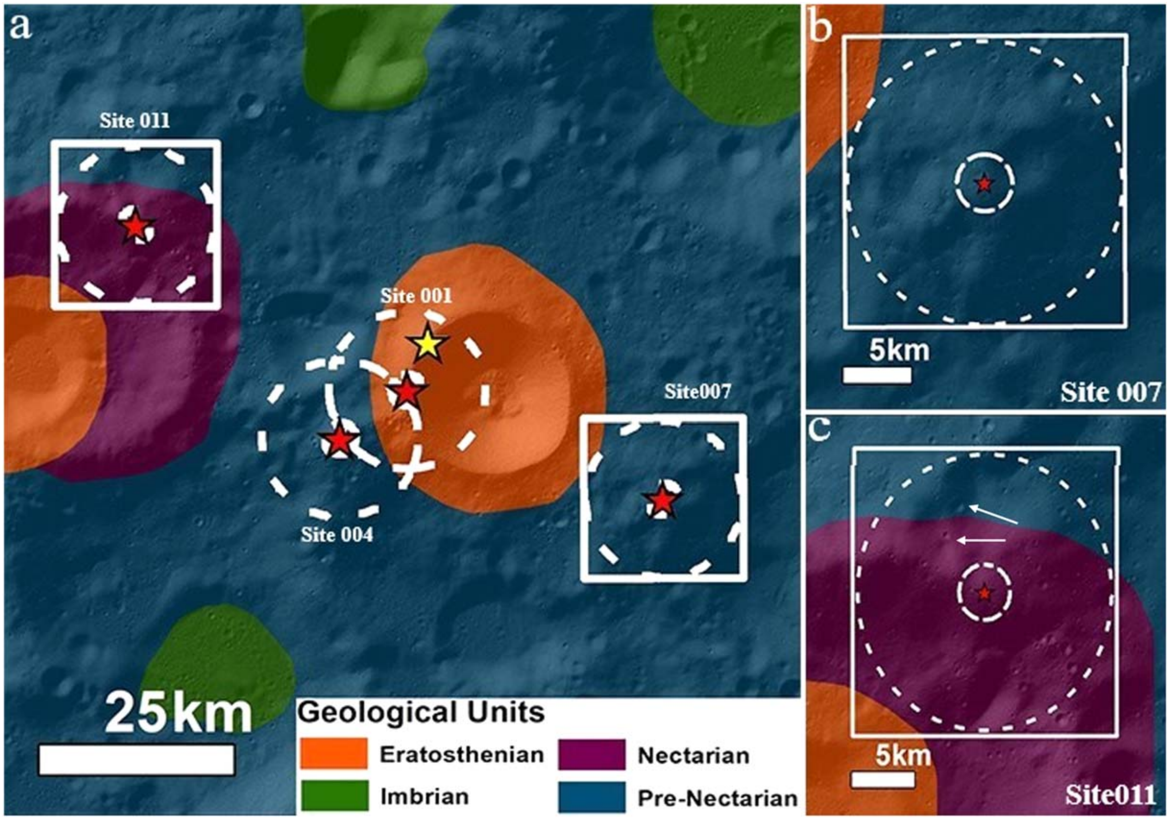

Figure 2. (a) Geological units in the south pole region of the Moon mapped by USGS Astrogeology Science Center et al. (2013). (b) Close view of Site 007 with pre-Nectarian material. (c) Close view of Site 011 with Eratosthenian, Nectarian, and pre-Nectarian material. The arrows indicate potential Orientale secondary impacts.

ring of massifs, covered with SPA ejecta, that were, in turn, buried by ejecta from younger impact events (Spudis et al. 1994, 2008). The basin was generated by an impact with an energy of $\sim 4 \times 10^{26}$ J (Potter et al. 2012) that removed the lunar crust from the center of the basin, replacing it with a large melt sheet that may have subsequently differentiated (Vaughan & Head 2014; Hurwitz & Kring 2015). The central peaks of younger craters produced within the basin after the melt sheet solidified consist of noritic material, and a thin layer of gabbro/basalt is distributed over large plains in the basin (Borst et al. 2012; Kramer et al. 2013). Moriarty & Pieters (2018) further characterized the basin into two pyroxene-bearing zones (roughly covering the central portion of the basin) and a surrounding annulus that is compositionally heterogenous. One of the central pyroxene-bearing zones is composed of anomalous Ca/Fe-rich pyroxene associated with the deepest portion of the SPA basin. The region surrounding this is rich in Mg-rich pyroxene further surrounded by the heterogenous annulus composed of a mixture of feldspathic and mafic material.

The margins of the basin, where sites 007 and 011 are located, have been identified as a feldspathic highland terrain, similar to the terrain at the Apollo 16 landing site. Sites 007 and 011 are among a range of massifs that are generally understood to be blocks of lunar crust that were uplifted by the SPA impact event (Spudis et al. 2008). In the upper walls of the Shackleton crater, which lies between sites 007 and 011, anorthosite signatures (Ohtake et al. 2009; Yamamoto et al. 2012), consistent with the expected crustal composition based on the lunar magma ocean model (Wood et al. 1970), were detected and later correlated with rock exposures (Kring et al. 2020c, 2020d; Gawronska et al. 2020; Halim et al. 2021).

The topographically high sites 007 and 011 may overlay an anorthositic crust. The region is intensely cratered, so the surface has been repeatedly blanketed by impact ejecta. A series of these ejecta layers are exposed in the walls of the Shackleton crater (Gawronska et al. 2020) $\sim$12 km from Site 007. That sequence of material may also be found at or around Site 007 and potentially Site 011.

The SPA basin formed $\sim$3.9 to $\sim$4.3 billion years ago (Spudis et al. 2008; Morbidelli et al. 2012; Potter et al. 2012; Fassett & Minton 2013). Both the sites host a range of materials varying from pre-Nectarian to Eratosthenian (Figures 2(a)–(c)). Large impact craters in the immediate vicinity of sites 007 and 011 are younger. Site 007 is on a summit between the Slater crater (with an age of $3.8^{+}_{-}0.1$ Ga ; Deutsch et al. 2020), and the Shackleton crater (with an age of $3.15^{+0.05}_{-0.08}$Ga; Tye et al. 2015; Deutsch et al. 2020). A recent recalibration of the age of Shackleton gives an estimate of $3.43^{+0.04}_{-0.05}$Ga (Kring et al. 2021). The recalculation of age does not alter our calculations of ejecta layer thickness (see Section 4.5.2), as Shackleton remains the youngest crater with both of the estimated ages. Site 011 sits on the rim of the de Gerlache crater, which was excavated $3.9^{+}_{-}0.1$ Ga ago (Deutsch et al. 2020). Each of the sites have been modified by the addition of younger impact ejecta deposits. In the case of Site 007, ejecta from Shackleton and Slater may cover the area. In the case of Site 011, ejecta from Shackleton, Cabeus, and de Gerlache is possibly present. Impact cratering continues to the present day and continues to modify the uppermost regolith at both sites.

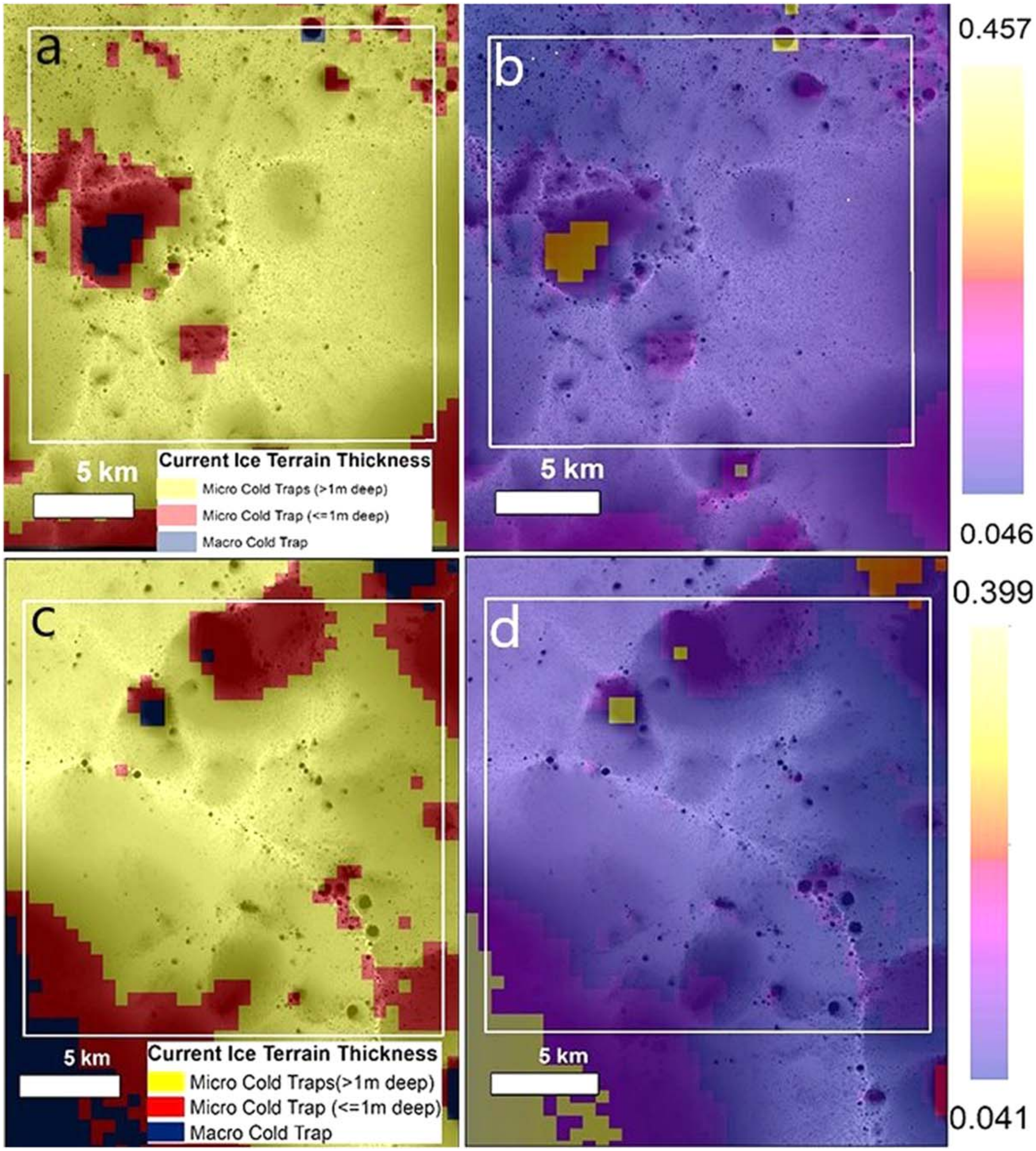

Figure 3. (a) Current ice terrain thickness in Site 007. (b) Ice favorability index of different locations within Site 007. (c) Current ice terrain thickness in Site 011. (d) Ice favorability index of different locations within Site 011 (Cannon & Britt 2020).

Both sites 007 and 011 are surrounded by craters that may have retained volatiles for billions of years (Elphic et al. 2007; Hurley et al. 2012). A recent study by Cannon & Britt (2020) examined the changes in location of such volatile deposits after true polar wander (Siegler et al. 2016), and produced maps that show the favorability of the presence of ice in these sites along with the depths at which ice may be found. This was termed as the ice favorability index (IFI), while an ice terrain thickness (ITT) map represents the probability of the presence of ice at different depths post-true polar wander (Siegler et al. 2016; Cannon & Britt 2020). Both sites encompass locations where ice deposits could be present on the surface, in the regolith within 1 m of the surface and beyond depths of 1 m from the surface (Figures 3(a)–(d)).

3. Data Set and Methods

A morphological study of the surface and mapping of boulder distribution utilized the high-resolution LROC Narrow Angle Camera (NAC) images with a resolution of $\sim$0.3 m px^{-1} to $\sim$1 m px^{-1} (Robinson et al. 2010). Quickmap[7] was used to identify NAC images with the highest resolution and varying illumination conditions that were then processed using the USGS's Planetary Image Locator Tool (Bailen et al. 2013). NAC south polar mosaic tiles, available from the LROC website, were used to generate figures in this paper.

Boulder distribution mapping at both study sites was completed at a scale of 1:800 in ArcMap, and the resulting

[7] https://quickmap.lroc.asu.edu

data were used to generate density maps and size distribution plots. Results were compared with boulder density and size distribution from the South Ray crater, an Apollo 17 landing site, available from the supplementary data of Watkins et al. (2019). To enable size comparison between the sites, the boulder diameter values from Watkins et al. (2019) were used.

Topographic analysis was carried out using Lunar Orbiter Laser Altimeter (LOLA) digital elevation models (DEMs) of resolutions from $\sim$5 m px^{-1} to $\sim$20 m px^{-1} (Smith et al. 2010, 2017; Barker et al. 2021) with a vertical uncertainty of $\sim$0.3 to 0.5 m for the 5 m px^{-1} data set. The average solar illumination at each site was examined using $\sim$60 m px^{-1} maps created by Mazarico et al. (2011). Existing maps of PSRs (Mazarico et al. 2011) near the south pole were used in the study. The data are available in the Planetary Data System (PDS) archive. The ITT map ($\sim$590 m px^{-1}) and IFI map ($\sim$590 m px^{-1}) used here are available from Siegler et al. (2016) and Cannon & Britt (2020). Temperature variation across the sites was studied using polar seasonal temperature maps ($\sim$240 m px^{-1}) created from data collected by the Diviner Lunar Radiometer Experiment (Diviner). The fraction of time the surface temperature is below 110 K map ($\sim$240 m px^{-1}) is available at the Diviner website (Williams et al. 2019). The Lunar Reconnaissance Orbiter (LRO) orbits the Moon making observations on both the day- and nightsides, separated by 180° longitude. The "time" in these maps has been expressed in hours by normalizing the angular distance between the subsolar and the geographic longitude to a 24 hr day (where daytime is between 6 a.m. and 6 p.m. and nighttime is between 6 p.m. and 6 a.m. local time; Siegler et al. 2011).

The ejecta thickness at each site was estimated at intervals of 500 m from the source crater rims using empirical equations (Kring 1995). ArcMap was used to measure the distance from the small, younger craters to the major impact craters in order to determine their relationship to underlying ejecta layers. QGIS was used to create contours to aid in estimating the depths of these smaller craters. These parameters were combined to determine the depths of crater excavation and further, the underlying layers of ejecta that were excavated by the smaller impacts and may be exposed at the surface.

As illumination is higher during the summer, lunar seasonal cycles were modeled using the Lunar Season Calculator (Cartwright & Bretzfelder 2021) to identify the dates in 2024 (planned launch for Artemis III) ,which correspond to summer in the southern hemisphere. Simulations were run over three lunar days (approximately three months) using tools within Moon Trek (Day & Law 2018), between 2024 December 1 and 2025 February 28 at 24 hr intervals. Resulting outputs were studied to identify windows during which the EZs receive maximum illumination. These outputs are limited, as the Moon Trek tools have not been optimized for the lunar poles. The results presented here provide a preliminary assessment of potential exploration windows under maximum illumination conditions.

4. Results

4.1. Topography and Slopes

Topographic variation within the sites is a key factor in determining both the amount of solar illumination received by the surface and the accessibility of different areas within the landing sites. Local slopes are an important factor in selecting landing sites and identifying traversable regions for exploration. The latest NASA's Human Landing System (HLS) requirement states that the HLS shall provide a vertical orientation of 0°–8° (threshold) and 0°–5° (goal) from local vertical for surface operations. The slope tolerance of HLS is expected to exceed the acceptable tilt angles for safe and effective execution of critical crew functions (NASA 2019). While landing terrain slopes greater than 15° can lead to overturn of a lander (De Rosa et al. 2012), slopes up to 25° have been recommended for crew rovers (Lunar Exploration Science Working Group 1995) based on rover performance and surface terrain during the Apollo 15, 16, and 17 missions. Such values have been used in previous landing site studies (Öhman & Kring 2012; Allender et al. 2019; Flahaut et al. 2020; Gawronska et al. 2020). The Apollo 12 and 14 missions consisted of walking EVAs up to 14° slopes. The specific capabilities of the Artemis exploration Extravehicular Mobility Unit are currently unknown (except those of the VIPER instrument)[8] and thus in this study we adopt the slope limits recommended by the Lunar Exploration Science Working Group (1995) and VIPER.

The LOLA DEM of Site 007 shows that the elevation varies by $\sim$2700 m within the site (Figure 4(b)), with the highest point being $\sim$1700 m above the lunar datum and the lowest being $\sim$1000 m below that datum. The contour map in Figure 4(b) shows that the area with the highest elevation appears to be the summit of a mound, potentially a part of the rim of an unnamed crater (Figures 4(a)–(b)) or pre-Nectarian massif (Figure 2), enveloped by the ejecta from younger impacts. It is located at the center of the site. The slopes within Site 007 are mostly below 25°, which could be safely traversed with a rover, except for a few regions on the crater walls (Figure 4(c)).

Site 011 has more dramatic topography than Site 007, even though the total variation in elevation of $\sim$2600 m is comparable to that of Site 007 (Figure 5(b)). Site 011 exhibits frequent variations in topography over short distances, and has overall steeper slopes relative to Site 007, as seen in the slope map (Figure 5(c)). The highest point of Site 011 is on the rim of de Gerlache crater with an elevation of $\sim$1400 m (Figures 5(a)–(b)). The walls of the de Gerlache crater constitute very steep slopes, well above 25°. (Figure 5(c)). There is, however, sufficient area (>50% within 2 km and 10 km EZ) connected by terrain with "safe" slopes (<15° for walking EVA and <25° for rover-facilitated EVA) in the region to permit traverses and exploration.

4.2. Surface Illumination and Earth Visibility

The illumination conditions at the poles were a major factor in preliminary selection of landing sites near the lunar south pole, especially given that the Artemis program intends to rely on solar power for surface operations. Regions with relatively higher average solar illumination (>50% of a lunar day) can be used for recharging solar powered cells and to conduct surface experiments (Bussey et al. 1999, 2005, 2010; Mazarico et al. 2011; Speyerer & Robinson 2013). Bussey et al. (2010) simulated the illumination conditions for the year 2020 using Kaguya laser data at the lunar south pole for locations around both Site 007 and Site 011, and estimated that these sites would receive maximum solar illumination during the first seven days of the south polar summer. Mazarico et al. (2011) used LRO-

[8] https://www.nasa.gov/viper/lunar-operations

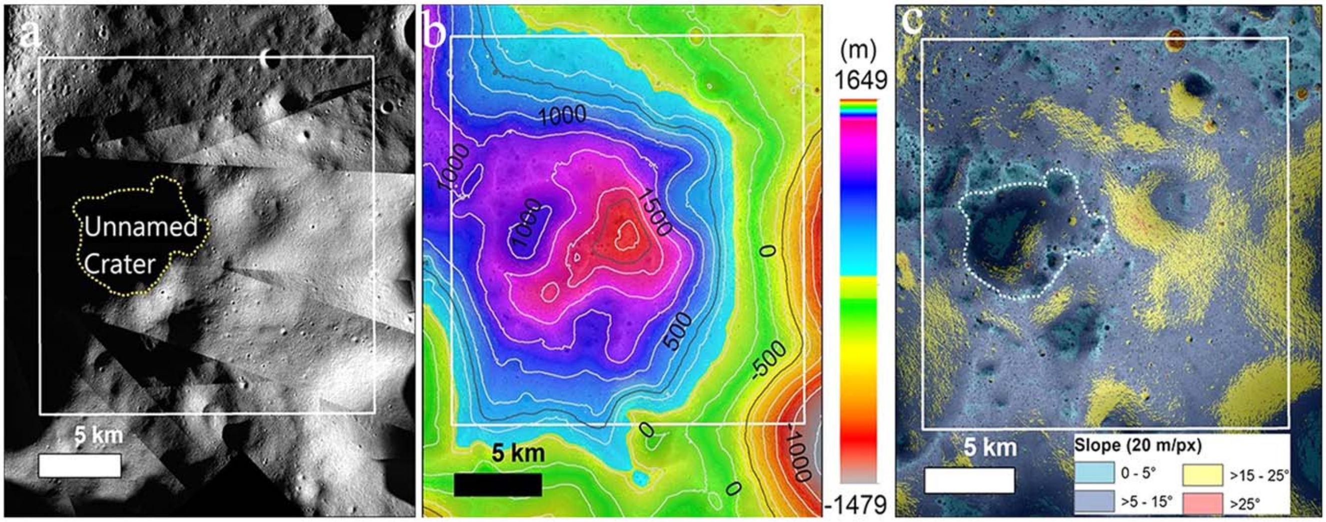

Figure 4. (a) LROC-NAC mosaic ($\sim$1 m px^{-1}) of Site 007 with unnamed crater. (b) LOLA DEM ($\sim$20 m px^{-1}) of Site 007 with contours of interval 500 m overlaid on it. (c) Slope map of Site 007 (displaying nontraversable slopes in red) overlaid on average solar illumination map.

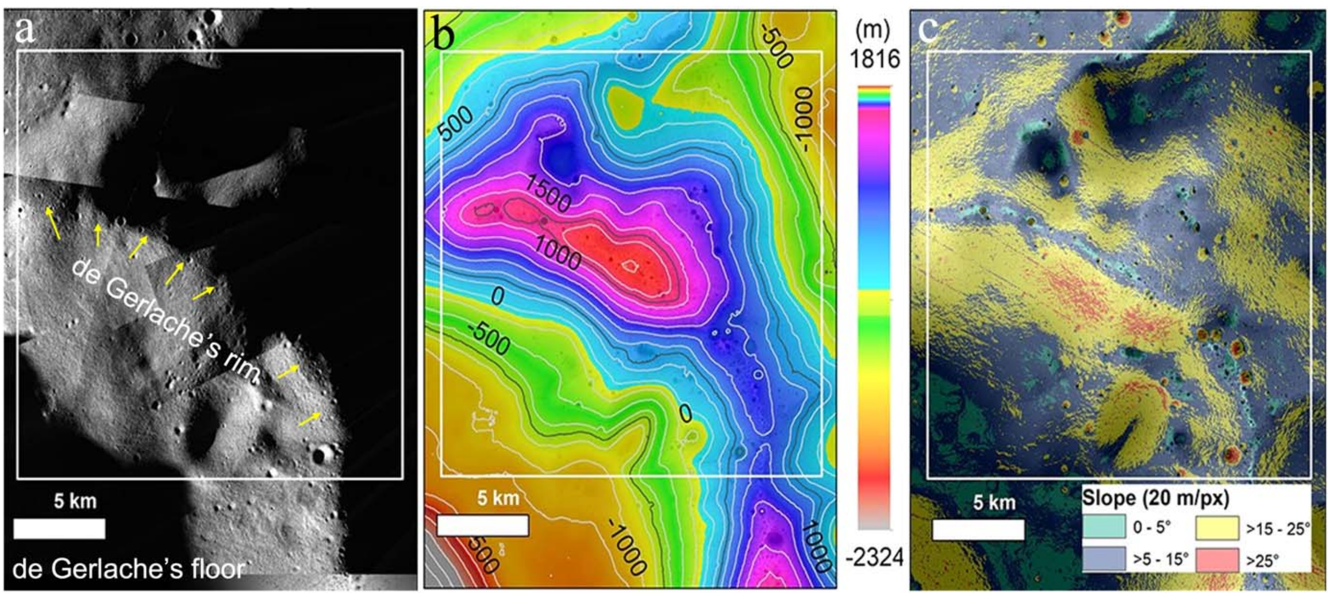

Figure 5. (a) LROC-NAC mosaic ($\sim$1 m px^{-1}) of Site 011. (b) LOLA DEM ($\sim$20 m px^{-1}) of Site 007 with contours of interval 500 m overlaid on it. (c) Slope map of Site 007 displaying nontraversable slopes in red color overlaid on average solar illumination map.

LOLA data, combined with a horizon method (using a DEM to store the elevation of the horizon in fixed directions and interpolate these fixed horizon elevations to a given Sun elevation to calculate the ratio of visible solar disk for a given location), further validated by LRO-Wide Angle Camera images, to generate an average solar illumination map over several lunar node precession cycles. The simulation run from 1970 to 2044 was used to compute the average solar illumination (Mazarico et al. 2011). Here the solar illumination was defined as the percentage area of the Sun's disk that is visible.

We used this map to evaluate the distribution of illumination beyond the point of highest illumination in each site, which is the central point around which the radial exploration areas are defined. The maximum average solar illumination at the central coordinates of both sites 007 and 011 is high (85.9% and 82.6%, respectively; Mazarico et al. 2011), but $\sim$3% and $\sim$4% of the area within 10 km radius of the site of highest illumination receives no solar illumination (Figures 6(a), (d)). Because the highly illuminated area is relatively small, most of the areas within the 2 km radial EZs at both sites receive only 30% to 50% average solar illumination (Figures 6(b), (e)). As we move out from the 2 km EZ to the 10 km EZ, solar illumination is reduced further to 10% in Site 011 (Figures 6(b), (e)). Because the other potential sites 001 and 004 have been ranked higher in terms of illumination at their central point, we also evaluated illumination at those sites within a 2 km walking EVA zone, the 8 km area outside the walking EVA EZ, and combined 10 km radial zones for rover exploration. We find that while the central 2 km portions of sites 004 and 001 have specific locations with higher illumination than 007 and 011, the sites overall do not receive higher illumination than 007 and 011 (Figure 6(c)). In fact, the region within 2 km of sites 007 and 011 on average receive higher illumination than Site 004 and comparable illumination to that of Site 001. Beyond a 2 km radial distance, in the 8 km

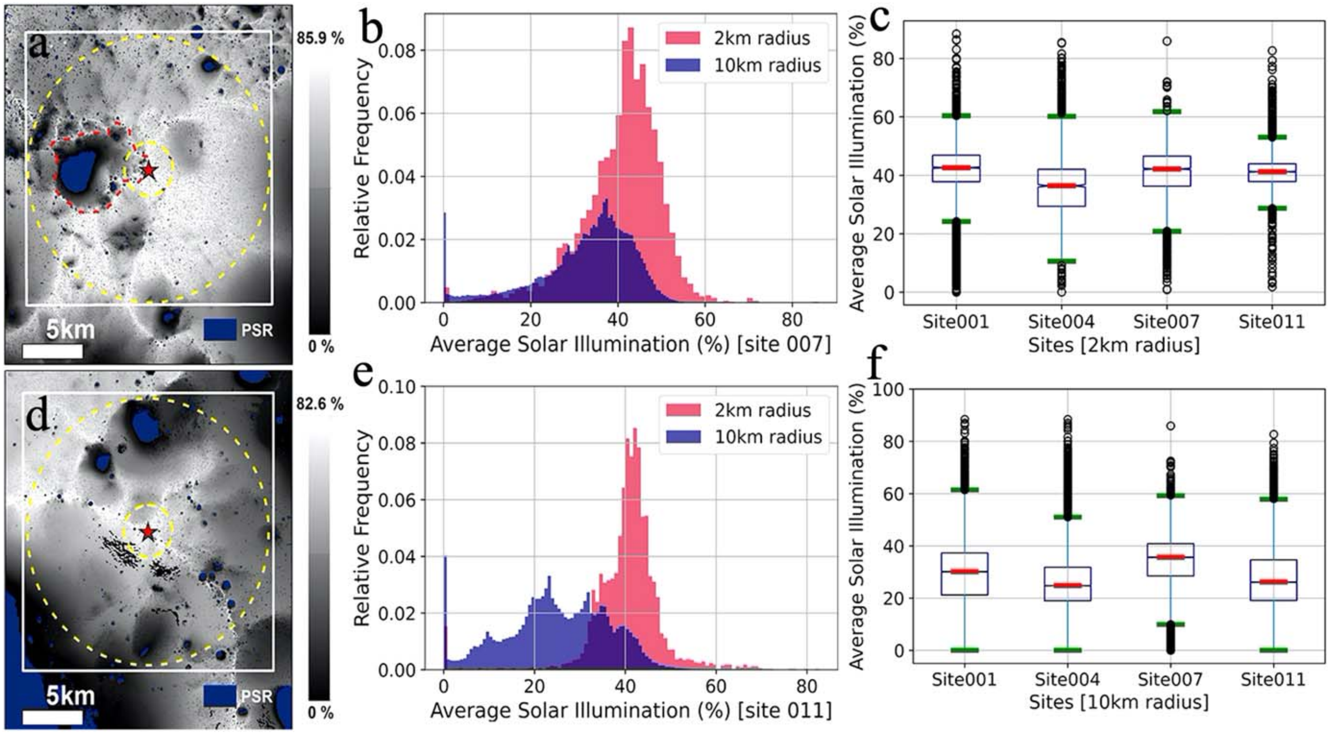

Figure 6. (a) Average solar illumination map with PSR overlay at Site 007 surrounded by 2 km and 10 km EZs (yellow dashed lines). The red star in the middle is the highest average solar illumination point. (b) Average solar illumination percentage within 2km EZ and outside it (excluding 2 km EZ) in Site 007. (c) Average solar illumination within 2 km EZ of sites 001, 004, 007, and 011. The beginning and end of the blue box represents the 25th and 75th percentiles of the values, and the pink line in the middle represents the 50th percentile (median). The green lines (or black dots) at the top and bottom are the maximum and minimum. The presence of black dots indicates that those values are outliers and more than 1.5 times of the 25th or 75th percentiles. (d) Average solar illumination map with PSR overlay at Site 011 surrounded by 2 km and 10 km EZs. (e) Average solar illumination percentage within 2 km EZ and outside it (excluding 2 km EZ) in Site 011. (f) Average solar illumination within 10 km EZ of sites 001, 004, 007, and 011.

Table 1
Dates During South Polar Summer 2024–2025 for Which the Exploration Areas are Illuminated Based on Moon Trek Outputs

Entire EZ		12/04/2024–12/09/2024	12/31/2024–01/08/2025	01/29/2025–02/06/2025	
Site 011	Eastern portion of EZ	12/13/2024–12/24/2024	01/11/2025–01/22/2025	02/10/2025–02/20/2025	
	Central portion of EZ	12/22/2024–12/24/2024	01/21/2025–01/22/2025	02/20/2025–02/21/2025	
	Western portion of EZ	12/01/2024–12/05/2024	12/24/2024–01/02/2025	01/23/2025–02/01/2025	02/20/2025–02/27/2025

Note. See Figure A1 for additional details on Site 011.

surrounding region, Site 007 receives the highest illumination, followed by sites 001, 011, and 004 (Figure 6(f)). Thus, while sites 001 and 004 may be more attractive if a stationary power station is installed or if their points of high illumination can be routinely accessed, however, it may be easier to maintain access to power at sites 007 and 011 during an initial survey of the polar region.

Due to the increase in both length and regional extent of illumination, the south polar summer would be the optimal season for surface operations. For the year 2024, the current planned launch time frame for Artemis III, this would correspond to 2024 December–2025 February. Illumination simulations completed using tools within Moon Trek indicate that the EZs will be well illuminated during the windows of time shown in Table 1. The entire EZ of Site 007 is well lit during three windows within the south polar summer of 2024–2025. In the same time frame, illumination moves across Site 011, illuminating the eastern, central, and western portions of the site during different dates (Table 1; see Figure A1 in Appendix A). Given current limitations on polar projections and simulations in Moon Trek, illumination conditions may be more favorable and extend over longer periods than is reflected in these results.

We also carried out an analysis of Earth illumination from the two sites to estimate the amount of time Earth will be visible from the sites in a lunar year. Our analysis shows that ∼50% of the area within the 2 km EZ in both sites will have Earth visibility for ∼50%–60% of the time. This reduces to ∼30% of the area for Site 007 and ∼20% of the time for Site 011 between the 2 km EZ and 10 km EZ boundaries (Figure A2 in Appendix A). This indicates that it might be possible to communicate directly to Earth from the landing regions of both sites for 60% of the time. For the rest of the time, and/or from other regions an orbital relay would be needed for communication.

4.3. Permanently Shadowed Regions

The Moon's axial tilt of 1.5° and the topography of its heavily cratered terrain produce long shadows at the poles, including PSRs. Though often found on the floors of large craters, PSRs are also present near uplifted crater rims and are

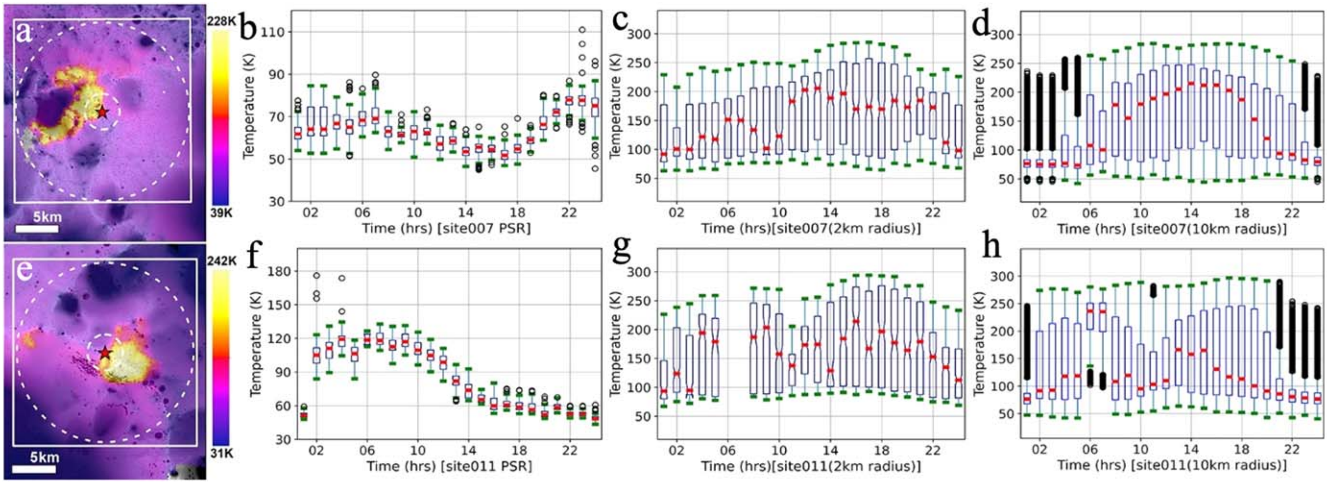

Figure 7. (a) Temperature map (at 11 a.m. local time) of Site 007 surrounded by 2 km and 10 km EZs. The red star in the middle is the highest average solar illumination point. (b) Temperature variation within the PSR in an unnamed crater in Site 007 over a lunar day–night cycle. (c) Temperature variation within 2 km EZ in Site 007 over a lunar day–night cycle. (d) Temperature variation outside 2 km EZ (within 10 km) in Site 007 over a lunar day–night cycle. (e) Temperature map (at 11 a.m. local time) of Site 011 surrounded by 2 km and 10 km EZs. The red star in the middle is the highest average solar illumination point. (f) Temperature variation within the two large PSRs in Site 011 over a lunar day–night cycle. (g) Temperature variation within 2 km EZ in Site 011 over a lunar day–night cycle. (h) Temperature variation outside 2 km EZ (within 10 km) in Site 011 over a lunar day–night cycle.

widespread in smaller craters (Bussey et al. 1999, 2003, 2010). Being sufficiently "old and cold," these PSRs could host H_2O and other volatiles that accumulated through various indigenous and exogenous transportation mechanisms (Prem et al. 2015). Endogenous mechanisms include volcanism (Needham & Kring 2017; Kring et al. 2021) and degassing from the planet's interior (Taylor et al. 2018), while exogenous sources are solar wind (Arnold 1979; Crider & Vondrak 2003), asteroid and comet impacts (Morgan & Shemansky 1991; Stewart et al. 2011), and potentially giant molecular clouds (Lucey 2009; Lawrence 2017). Analyses of the stratigraphy and composition of any ice deposits will, thus, provide a measure of the evolution of volatiles in the inner solar system over billions of years. PSRs may also have special surface charging, space plasma effects, and distinct surface density due to regolith-volatile mixing (Schultz et al. 2010) that may affect exploration strategies. Using a PSR map prepared by Mazarico et al. (2011) we evaluated the extent and distribution of PSRs at the two sites and how they might be incorporated as targets for surface EVAs.

Within 10 km of Site 007, there is a large PSR on the floor of a ∼5 km diameter unnamed crater (Figure 6(a)). Hillshade images (generated from LOLA topographic data) indicate a landslide blankets one side of the crater (Figure A3 in Appendix A). The PSR on the floor of this unnamed crater covers an area of $\sim 7.3\ km^2$, and there has been a direct detection of water ice in the PSR within this crater by Li et al. (2018) using the visible and near-infrared data set from the Moon Mineralogy Mapper. Other PSRs within other small craters cover a total area of $\sim 0.0396\ km^2$ within the 2 km EZ.

The largest PSR near Site 011 is located on the floor of the de Gerlache crater, but it not accessible due to the steep crater walls (slopes >25°) and a distance >10 km from the central point of Site 011 (Figure 6(d)). However, several small craters on the rim of de Gerlache and two larger craters beyond the rim (the latter being potential secondaries from the Orientale impact) host accessible PSRs. The PSRs in small craters within 2 km radius cover a total of $0.108\ km^2$ while those in the larger secondary craters within the 10 km radial limit cover an area of $\sim 6.05\ km^2$. The average solar illumination map of the lunar south pole suggests that, aside from the topographic highs, most other regions receive generally low solar illumination.

4.4. South Pole Temperature During Summers and Micro-cold Traps

Ideally, collected polar samples that may contain volatiles would remain pristine (without undergoing phase changes or diffusion) throughout their return to Earth. Thus, in order to prepare for sample return, it is important to understand the surface temperature distribution at the potential collection sites. The diurnal temperature distribution will also aid in selection of the optimal instrumentation for surface science, including studying the current stability and the rate of volatile flux at the PSRs. The thermal cycle may also influence regolith porosity and stability in these areas, which can have implications for the safety of the walking and roving EVAs.

It is also important to analyze the diurnal temperature in these sites to account for sudden temperature changes, which might drive requirements for the design of vehicles and habitats such that they withstand the effects of thermal expansion and contraction.

To study the temperature variation at sites 007 and 011, we used temperature maps prepared using ∼10 yr of Diviner data (Williams et al. 2019) over 24 hr intervals during south polar summers. Using temperature maps of the 2 km radial EZ we observe that, unlike the equatorial region, the temperature maxima occur at 5 p.m. local time for both sites 007 and 011. The minimum in this region occurs at 1 a.m. for both sites (Figures 7(c), (g)). For the regions beyond the 2 km radius, we observe maxima and minima for Site 007 at 11 a.m. and 12 a.m., respectively, and for Site 011 at 5 p.m. and 5 a.m., respectively (Figures 7(d), (h)). The variation in maxima and minima temperature of Site 011 in the 2 km versus 10 km EZ be explained by the presence of large PSRs outside the 2 km EZ and a decrease in amount and duration of solar illumination. Although the maximum and minimum temperatures do not change drastically at either site, we observe significant variation in the median temperatures of both sites. This means

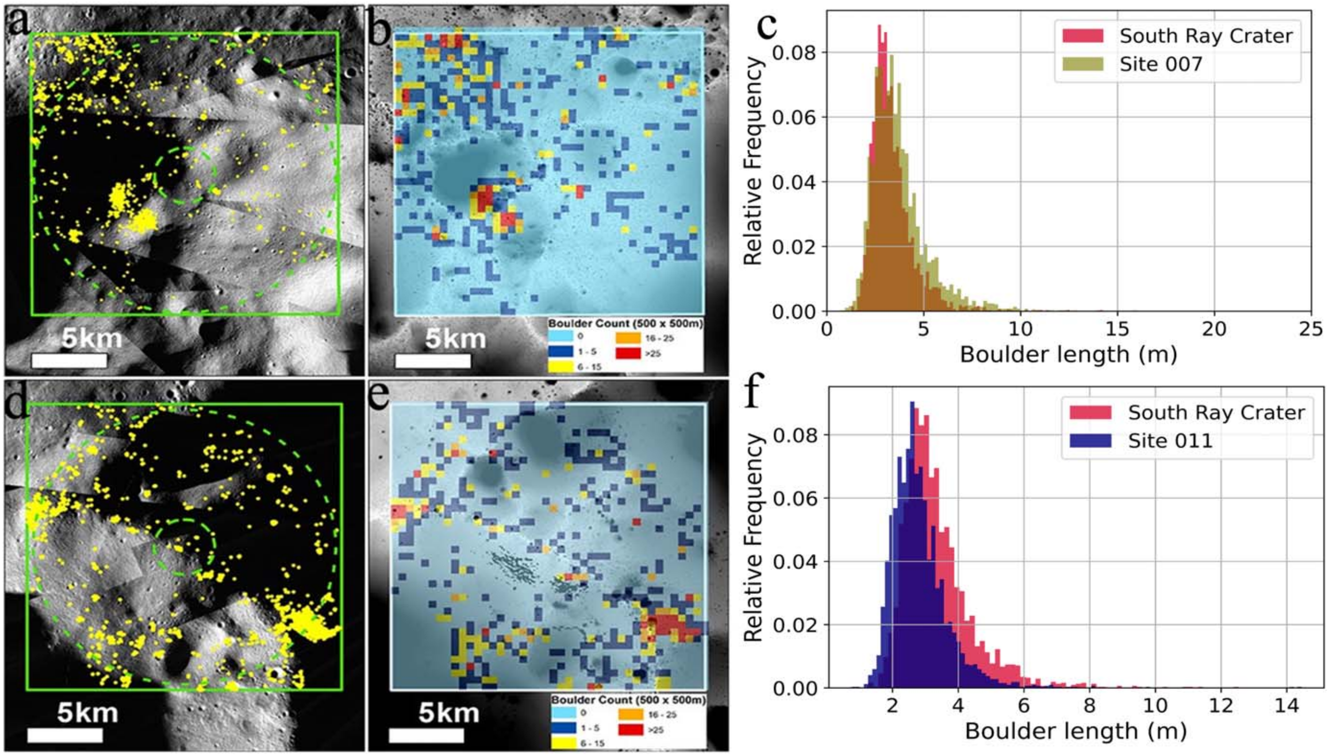

Figure 8. (a) Boulder locations (yellow) overlaid on NAC mosaic within Site 007. (b) Boulder density distribution (500 × 500 m) of Site 007 overlaid on average solar illumination map. (c) Comparison of boulder lengths in Site 007 with the South Ray crater. (d) Boulder locations (yellow) overlaid on NAC mosaic within Site 011. (e) Boulder density distribution (500 × 500 m) of Site 011 overlaid on average solar illumination map. (f) Comparison of boulder lengths in Site 011 with the South Ray crater.

that, though there are small regions with more extreme temperature variations, the majority of area within these sites lies approximately between 70 K and 200 K (Figures 7(c), (d), (g), (h)). We also plotted (Figures 7(b), (f)) daytime temperature changes in summers of the largest PSR within Site 007 (area 7.3 km^2; refer to Figure 6(a)) and two small PSRs within Site 011 (area ∼6.05 km^2; refer to Figure 6(d)). We observe that the PSR inside the unnamed crater at Site 007 displays a sinusoidal rising and falling of temperature with two maxima at 7 a.m. and 11 p.m. (Figure 7(b)). The two PSRs in Site 011 display temperature maxima in the morning at 3 a.m. and then gradual decline throughout the day (Figure 7(f)). Temperature variation within the two PSRs at Site 011 over a lunar day–night cycle are due to secondary illumination from the crater walls. Beyond these PSRs there exist regions that remain below 110 K for varying lengths of time per year. These areas serve as favorable locations for seasonal volatile accumulation and are known as seasonally shadowed regions (SSRs). A study by Kloos et al. (2019) indicates that the expansion of these regions peak around ∼80 days from northern vernal equinox, and the water retention in these SSRs exhibit a seasonal retention peak near the hemispherical vernal equinox rather than the solstice. Here we used an average SSR map prepared by Williams et al. (2019) to evaluate the boundaries of the regions remaining below 110 K throughout the year (Figure A4 in Appendix A). In sites 007 and 011, ∼15% of the total area (12.56 km^2) within the 2 km radial EZ remains under 110 K for ∼40% of the year. This increases to ∼60% of the time in the 10 km radial EZ (Figure A1). These areas are generally present around PSRs and tend to expand due to low solar illumination after the northern vernal equinox. In the event that extensive boulder fields or steep (>25°) slopes prevent access to large PSRs, these SSRs may provide alternative areas for volatile exploration and in situ resource utilization (ISRU). Large boulders also form long shadows, creating potential micro-cold traps, similar to Shadow Rock at the Apollo 16 landing site (Gawronska et al. 2020). A recent study by Hayne et al. (2021) suggests small-scale shadows (<100 m in diameter) remain constant in the polar regions of the Moon, unlike larger ones, which change with time. Their model implies that approximately ∼10% to ∼20% of permanently trapped water may be found in these micro-cold traps. Spatially, they cover an area of ∼24,000 km^2 poleward of 80°S and could serve as another, more accessible alternative to larger PSRs for scientific and ISRU purposes.

4.5. Geological Diversity of the Sites

4.5.1. Boulder Distribution at the two Sites

Impactors that hit bedrock covered by a thin layer of regolith will tend to excavate boulders (Hartmann 1969; Gault et al. 1972; Hörz et al. 1975; Watkins et al. 2019). In these cases, boulders can be used to sample the bedrock, especially in situ ations in which the bedrock is not otherwise exposed or accessible. In addition, the boulder density and size distribution in a region can increase our understanding of regolith formation on the Moon. Boulder size and density distributions can serve as an indicator of the mechanical strength of the terrain (Basilevsky et al. 2015; Watkins et al. 2019). The boulder density can also be used to identify hazardous regions for landing and exploration purposes, as regions with high boulder densities may present additional challenges. Here, we mapped visible boulders at both sites to identify potential hazards and

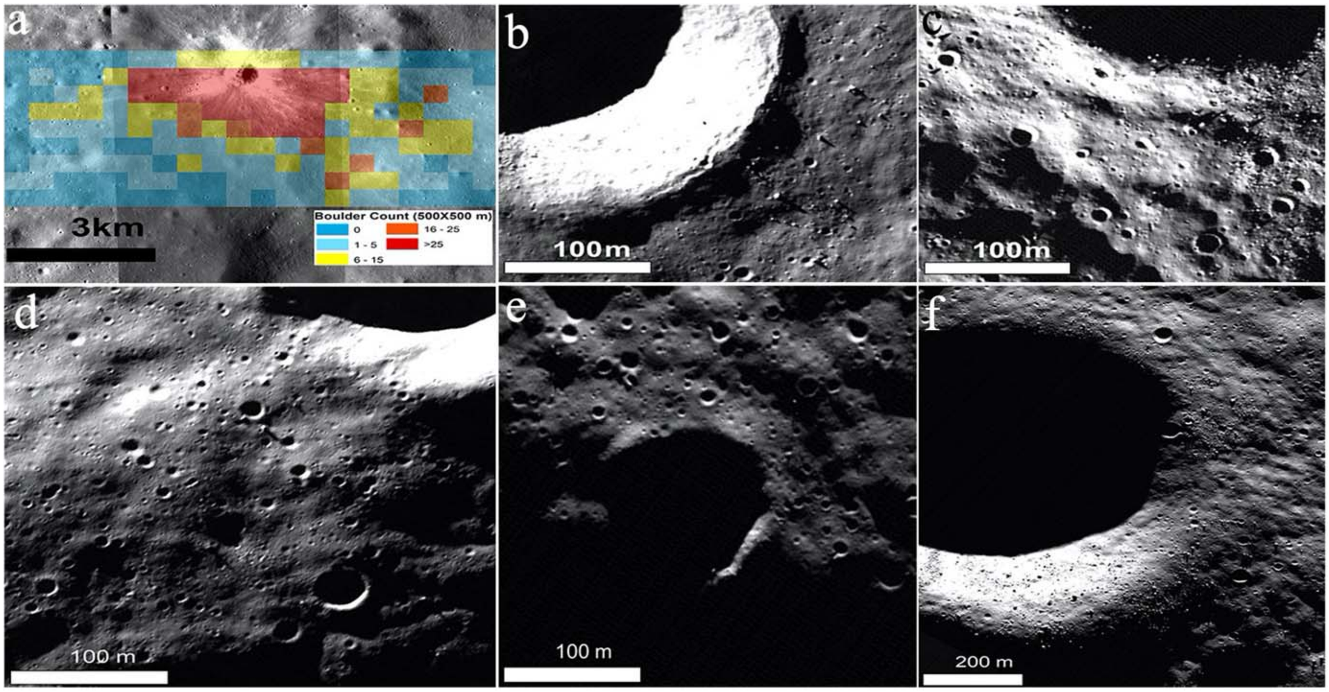

Figure 9. (a) Boulder density distribution (500 × 500 m) of the South Ray crater overlaid on NAC images. (b)–(c) Close view of boulders in Site 007. (d)–(f) Boulder along the rim of the de Gerlache crater in Site 011.

science sampling targets using NAC image strips of highest resolution (~0.3 m px^{-1} to ~0.7 m px^{-1}) in the area. A total of 3204 resolvable boulders were mapped within 10 km around Site 007 and 3774 boulders around Site 011 (Figures 8(a), (d)). Though boulders were seen on crater walls and/or at the base of steep slopes, no tracks were identified at either site. At the Apollo 16 site, a boulder with an exposure age of 22 Ma (Arvidson et al. 1975) has a track, while a boulder with an exposure age of 28 Ma does not, implying tracks are resurfaced on a timescale of roughly 25 million years (Hurwitz & Kring 2016; Kumar et al. 2016). Thus, the boulders at sites 007 and 011 without tracks may be older.

The resulting boulder density distribution maps are shown in Figures 8(b) and (e) and size distribution plots in Figures 8(c) and (f). The boulder density distribution was defined as the number of boulders present in a given area. Boulder density distributions per 250 m × 250 m, 500 m × 500 m, and 1 km × 1 km were calculated for both sites. The density distribution varies from areas with zero boulders per km^2 to more than 100 boulders per km^2.

Boulder fields are often concentrically concentrated around craters, as would be expected if they are debris excavated during impact events. The observed boulder density is relatively high near the larger PSRs in both sites. The top-left quadrant of Site 007 (toward the Shackleton crater; Figure 8(a)) has a relatively high boulder density, which may indicate the presence of a high number of young craters. The bottom-left quadrant of the site (as oriented in Figure 8(a)) hosts a smaller number of boulders (Figure 8(a)). The size of the boulders varies between ~14 m and ~0.7 m (minimum detection limit) with an apparent mean of ~2.8 m at a standard deviation of 0.85 m. The presence of a substantial number of 4 to 9 m boulders is comparable to the boulders near the South Ray crater, a ~2 million-year-old crater (Arvidson et al. 1975) in the feldspathic highlands of the Apollo 16 site (Figures 9(b)–(c)).

The boulders in Site 011 are primarily concentrated around the rim of the de Gerlache crater. We also observed boulders in the vicinity of young craters and on the walls of the de Gerlache crater. The boulder density of Site 011 seems to be relatively high along the rim and wall of the de Gerlache crater and around the PSRs (Figures 8(d)–(e)). Boulder dimensions vary from ~26 m to ~0.7 m (again, a minimum detection limit) with an apparent mean of ~3 ± 1.486 m (Figure 8(f)). Most of the boulders are in the ~3 to 4 m range along with a high number of boulders in the ~2 to 6 m range (Figures 9(d)–(f)) as displayed by the size density distribution map.

A comparison of boulder lengths with those around the Apollo 16 South Ray crater, which was excluded from EVA activity due to potential hazards, highlights the potential challenges of this terrain. However, the boulders provide valuable opportunities for science and exploration. We find that most of the boulders within Site 007 are roughly of the same size as the South Ray crater's (Figure 8(c)), while the boulders of Site 011 are smaller in size than those at the South Ray crater (Figure 8(f)). Thus, the boulder-rich regions in Site 007, especially near the PSR, could be difficult to traverse. However, if the boulder-rich terrain can be traversed, the large boulders excavated from depth near sites 007 and 011 would make sampling of subsurface material easier and may provide opportunities to assess layering representative of the local subsurface.

4.5.2. Ejecta Patterns at the two Landing Sites

Another approach used to characterize the geological diversity of the sites was via calculation of the thickness of

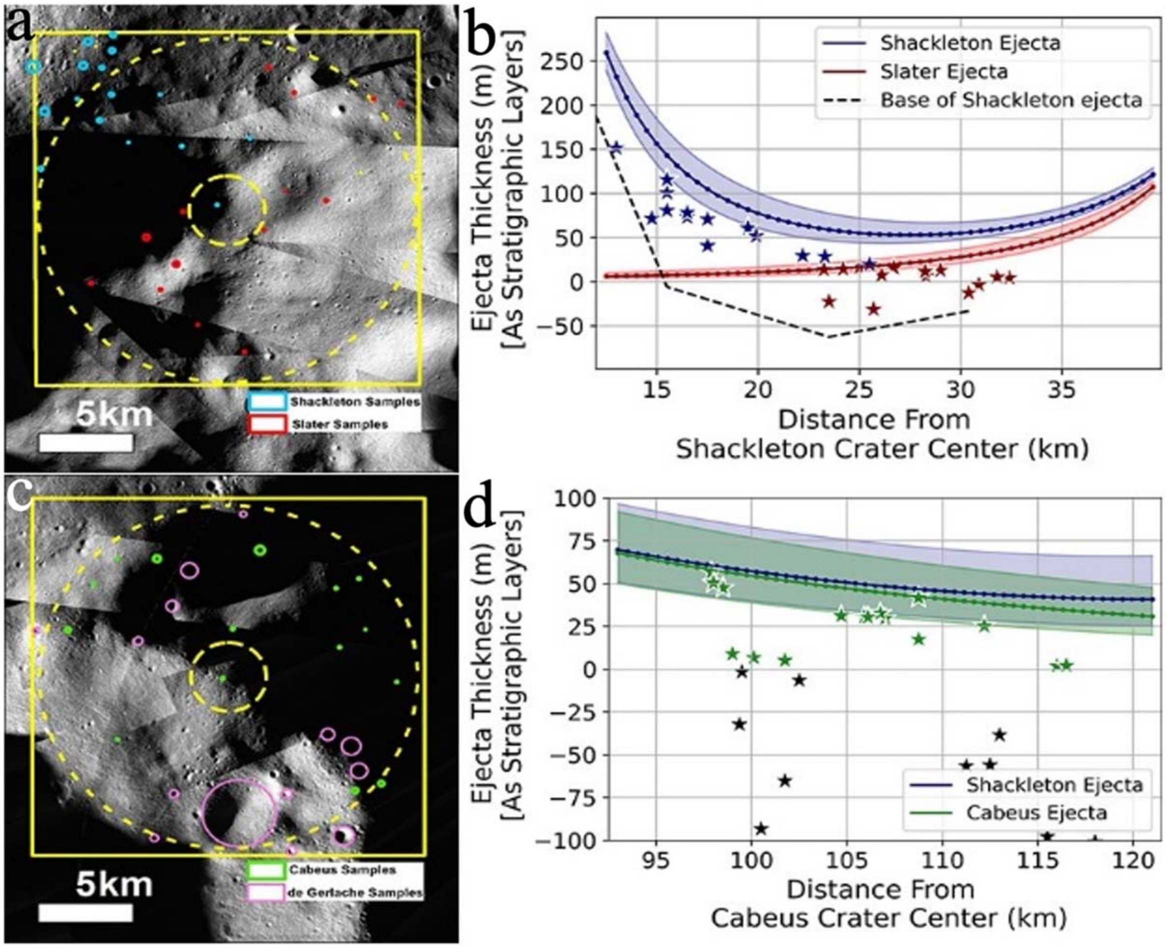

Figure 10. (a) Craters excavating Shackleton and Slater ejecta in Site 007. (b) Ejecta thicknesses of Shackleton and Slater craters on Site 007. Red points are the craters that excavated slater ejecta while blue points are the ones that have sampled Shackleton ejecta. (c) Craters excavating Cabeus and de Gerlache ejecta in Site 011. (d) Ejecta thicknesses of Cabeus and Shackleton craters on Site 011. Green points indicate the craters that excavated Cabeus ejecta and black points are the craters that ecavated de Gerlache ejecta.

the ejecta layers overlaying each site. We used the absolute model ages compiled and derived by Deutsch et al. (2020) to determine the chronology of impacts in the region that may have deposited ejecta at each site. Site 007 and Site 011 are surrounded by the Slater, Faustini, Shackleton, Shoemaker, de Gerlache, Cabeus, and Haworth craters. Of these seven, the four youngest, and those also sufficiently close to produce ejecta deposits, are the Shackleton, Slater, Cabeus, and de Gerlache craters. Crater ages were used to define the stratigraphy of ejecta at the two sites. Site 007 is bounded by Slater ($3.8 \pm 0.1\ Ga$) on the right and Shackleton ($3.15^{+0.05}_{-0.08}$Ga) to its left. Since Slater is older, its ejecta would have been buried by the ejecta from Shackleton. Faustini and Shoemaker, being older and farther from the study sites, had relatively low influence on the material present at this site. In the cases of other impacts, the ejecta thicknesses have been found to be $<$5 m thick with negative values for lower and upper bound of scaling exponents (e.g., Sverdrup) and thus are not considered for our study.

The ejecta thicknesses from Shackleton, Slater, and de Gerlache at sites 007 and 011 were estimated using empirical relationships between distance and crater diameter for simple and complex craters (Kring 1995):

$$\delta = 0.04 R_s \left(\frac{r}{R_s}\right)^{-3.0 \pm 0.5}$$

$$\delta = 0.14 R_c^{0.74} \left(\frac{r}{R_c}\right)^{-3.0 \pm 0.5},$$

where δ is the ejecta thickness, r is the distance from the point of impact, R_s is the radius of a simple crater, R_c is the radius of a complex crater, and all values are in meters. The Shackleton crater (21 km diameter) is a simple crater while Slater (25 km diameter), Cabeus (101 km diameter), and de Gerlache (31 km diameter) are complex craters.

Site 007 lies between ∼12.5 km and ∼40 km from the center of the Shackleton crater and between ∼14 km and ∼36.5 km from the center of Slater (details in Tables B1 and B2; Appendix B). The ejecta thickness from Shackleton at Site 007 is estimated to range from ∼249 m to ∼8 m thick (Figure 10(b)) across the site, and that from Slater is estimated to be between ∼107 m and ∼6 m deep (Figure 10(b)). The ejecta layer from Slater is thinner than that from Shackleton

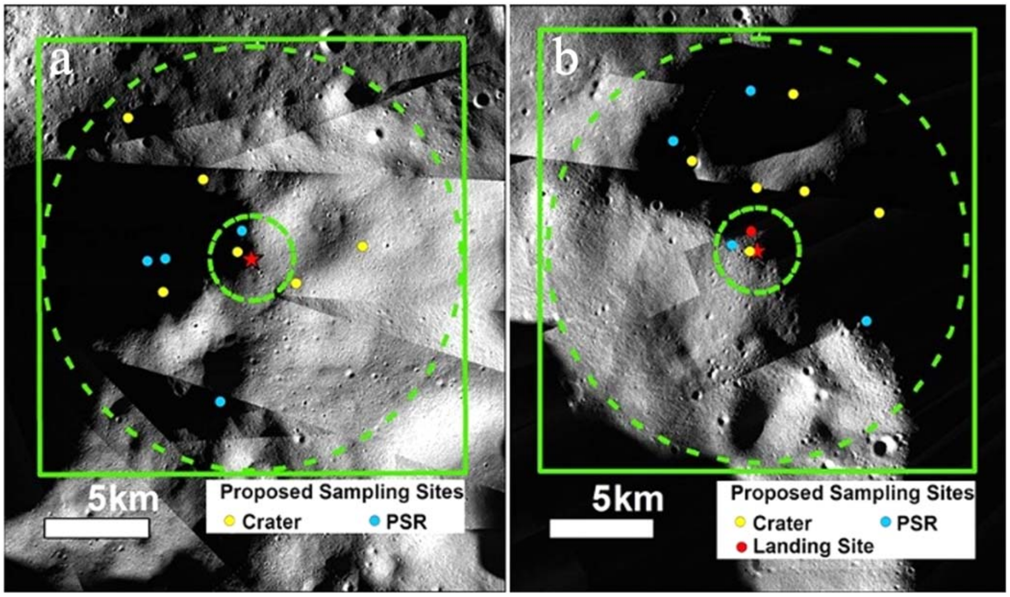

Figure 11. (a) Proposed sampling locations within Site 007. (b) Proposed sampling locations within Site 011.

throughout the area because the crater center lies farther away from the site. In a similar manner, we observe that the ejecta thickness of Slater is relatively higher in the region closer to the point of impact (away from Shackleton, as seen in Figure 10(b)) and the ejecta thickness of Shackleton is relatively higher on the opposite edge of the site (near Shackleton).

As shown in Figure 1, Site 011 is bounded by the Shackleton crater to the right, the Cabeus crater (3.8$\pm$0.1 Ga) at the top, and lies partly on the walls of the de Gerlache crater (3.9$\pm$0.1 Ga). Other nearby craters such as Haworth are of pre-Nectarian age with minimal influence on ejecta covering the area. Site 011 lies between ~36.5 km and ~64 km from the center of Shackleton, ~92.5 km and ~121.5 km from the center of Cabeus, and up to ~30.5 km from the center of de Gerlache (Figure A5 in Appendix A). The calculated thickness of Shackleton ejecta on the site varies from ~10 m to ~2 m; ejecta from Cabeus crater may be ~68 m to ~31 m deep (Figure 10(d)); and material from de Gerlache ranges from ~185 m to ~31 m (details in Figures 10(c)–(d), Figure A4, and Tables B1, B3, and B4). The sequence of events indicates the site is covered by proximal ejecta of de Gerlache, followed by debris from the more distant Cabeus and Shackleton impact sites, respectively. The ejecta thickness of Shackleton is relatively low on the site due to the distance from the crater center, while the thickness of de Gerlache ejecta is highest due to the site's location adjacent to the crater rim.

Excavated debris around craters, including boulders, are potential sampling sites. In a region of overlapping ejecta blankets, it is important to assess excavation depths and, thus, potential sources of ejected debris. Excavation depths of 30 craters were calculated to determine whether they only sampled debris from the topmost ejecta layer or if they also excavated material from deeper ejecta layers. For those craters that penetrated the Shackleton ejecta blanket, we compared crater depths with modeled ejecta thicknesses from Halim et al. (2021) and Gawronska et al. (2020). The depths of craters around Site 007 vary from ~80 m to ~5 m and their diameters vary from ~621 m to ~39 m, with depth/diameter values of ~0.1 to ~0.3. Around Site 011, crater depths vary from ~930 m to ~4 m for craters with diameters ranging from ~3.9 km to ~27 m (Table B5, Appendix B), with depth/diameter values of ~0.1 to ~0.3. Based on these calculations, 15 craters around Site 007 may have penetrated the Shackleton ejecta blanket and excavated underlying material from the Slater crater's ejecta (Figure 10(a)), and the base of at least one crater lies very close to the base of the Shackleton ejecta blanket (Figure 10(b)). In addition (Table B6, Appendix B), 14 craters may have excavated de Gerlache ejecta, and 16 craters may have sampled Cabeus ejecta at Site 011 (Figure 10(c)).

5. High-priority Locations for Sampling

The data and calculations collated above provide a baseline for considering potential scientific and ISRU targets if an EVA were to occur at either Site 007 or Site 011. Shackleton crater ejecta may contain Shackleton impact melts, from which an age can be ascertained (Kring 2019), which currently is estimated to be $3.43^{+0.04}_{-0.05}$ Ga (Kring et al. 2021). The ejecta may also contain impact melt from SPA and other pre-Nectarian- and Nectarian-age impacts, cryptomare from the SPA, and fragments of the original highland crust, with components from the lunar magma ocean and later intrusive rocks. As noted in Section 2, the Shackleton crater excavated anorthosite from the ancient lunar crust, plus a sequence of older impact ejecta horizons (Gawronska et al. 2020; Halim et al. 2021). de Gerlache and Cabeus ejecta may contain plagioclase and a mixture of low-calcium pyroxene and olivine (Blalock et al. 2020; Lemelin et al. 2021).

5.1. Site 007 and Site 011

Using NAC images (Robinson et al. 2010), maps of slope, boulder distribution and average solar illumination (Mazarico et al. 2011), PSRs (Mazarico et al. 2011), IFI and ITT (Cannon & Britt 2020), direct water detection points (Li et al. 2018), and calculated ejecta thicknesses, 10 locations were selected within the 2 km and 10 km EZs for each site to illustrate the diverse types of geological and volatile sampling available during an

Table 2
Details of Potential Stations Near Site 007

Name	Longitude	Latitude	Type	Diameter (m)	Significance	EZ
C1	123.86	−88.834	Crater	94.1	Excavates Shackleton ejecta & shows gully slumps	2 km
C2	123.37	−88.73	Crater	85.7	Excavates Slater ejecta	2.3 km
P1	122.3	−88.846	PSR	…	Potential young PSR	2 km
C3	133.15	−88.71	Crater	57.5	Excavates Slater ejecta & near high-IFI region	10 km
C4	118.79	−88.67	Crater	121.9	Excavates Slater ejecta & shows terraced slumps	10 km
C5	129.9	−88.89	Crater	290.2	Excavates slater ejecta	10 km
P2	127.7	−88.92	SSR	…	Direct water detection	10 km
P3	128.76	−88.94	PSR	…	Large PSR	10 km
C6	118.96	−89.09	Crater	208.08	Excavates Shackleton ejecta	10 km
C7	120.41	−88.94	Crater	121.51	Excavates Shackleton ejecta	10 km

Table 3
Details of Potential Stations Near Site 011

Name	Longitude	Latitude	Type	Diameter (m)	Significance	EZ
L1	−67.12	−88.65	Landing Site	…	Safer landing site away from hazardous boulder-rich region at point of highest illumination	2 km
C1	−68.38	−88.66	Crater	126.6	Excavates Cabeus ejecta	2 km
P1	−68.41	−88.63	PSR	…	PSR in a small, young crater	2 km
C2	−57.9	−88.61	Crater	462.4	Excavates Cabeus ejecta with slumps	10 km
C3	−70.02	−88.87	Crater	677.7	Excavates de Gerlache ejecta with PSR	10 km
C4	−64.61	−88.52	Crater	646.32	Excavates de Gerlache ejecta	10 km
C5	−64.37	−88.63	Crater	137.2	Excavates Cabeus ejecta	10 km
P2	−59.13	−88.55	PSR	…	PSR and potential sampling of Orientale ejecta	10 km
P3	−64.01	−88.48	PSR	…	PSR and potential sampling of Orientale ejecta	10 km
C6	−61.99	−88.82	Crater	110.5	Excavates potential Shackleton and Cabeus ejecta	10 km
P4	−63.12	−88.7	PSR	…	PSR en route to C6	10 km

EVA (Figures 11(a)–(b)). The targets should be safely accessible from the central points of each site via paths along <25° slopes that avoid rough topography around small craters and boulder fields. The locations and their scientific and/or ISRU potential are itemized in Tables 2 and 3.

6. National Research Council of the National Academies (2007) Goals Fulfilled by Exploring Sites 007 and 011

In this section, we highlight the National Research Council of the National Academies (2007) goals that may be fulfilled by the proposed exploration targets near sites 007 and 011. Both areas would provide access to samples from which the radiometric ages of impact events can be derived, although assigning breccia clasts of melt or shock-metamorphosed material to a particular source crater may be difficult. Nonetheless, those ages would help craft a broad chronology spanning the oldest remnant basin-forming event (e.g., the SPA) to an impact (e.g., Shackleton) reflective of the post-basin-forming epoch. Interestingly, samples from Site 011 may contain ejecta from Orientale, potentially providing a measure of that basin's age and/or crustal samples from the western limb of the Moon. Those samples could address goals outlined in Concept 1 of the National Research Council of the National Academies (2007), such as providing a test of the lunar cataclysm hypothesis and anchoring the beginning of the basin-forming epoch by determining the age of the SPA. Deployment of in situ instruments measuring the thermal profile of the regolith and interior (beyond the top few microns currently measured by Diviner), regolith layering measured through radar, and potential crustal thickness measurements using seismometers can help in partially addressing the goals outlined in Concept 2 (e.g., characterizing the thermal state of the interior, etc.). Samples from PSRs can be used to address the goals of Concept 4 to assess volatiles; their sources; transport, retention, alteration, and loss processes; and physical properties of regolith mixed with volatiles. Concept 6, regarding determination of the structure of multiring impact basins, quantifying the effects of planetary characteristics on crater formation and morphology, and measuring the extent of lateral and vertical mixing, could be fulfilled due to the ability to study SPA materials through in situ measurement and core samples. Concept 7, focused on studying rare materials and space weathering, along with regolith modification processes, can also be addressed at these sites. Analysis of the local PSRs and the temperature variations within them can potentially fulfill the goals stated in Concept 8 (study of the release and migration of water vapor and other volatiles). The lunar poles are pristine and an ideal place to study the lunar atmosphere and dust environment, especially considering the potential presence of various volatile species.

7. Summary

Two potential Artemis landing sites in the lunar south polar region, known as sites 007 and 011(NASA 2020) were investigated to evaluate their potential for addressing key scientific objectives (National Research Council of the National Academies 2007) and ISRU experiments.

Site 007 is located 3 km from the rim of Shackleton and blanketed by Shackleton and Slater ejecta. Calculations suggest that the ejecta is between ∼270 and ∼10 m thick and may contain (1) impact melt from the Shackleton crater, pre-Nectarian material, and material from Nectarian basins; (2) cryptomare from the SPA basin; and (3) pure anorthositic rocks formed as a result of differentiation of lunar magma ocean, potentially augmented with other crustal lithologies such as noritic rocks (Yamamoto et al. 2012; Gawronska et al. 2020). Based on Site 007's location, the underlying material is likely to be crystalline terrain or layered terrain as identified by Gawronska et al. (2020). Several small (50–650 m diameter) craters puncture the Shackleton ejecta blanket and ejected 46 m boulders that can be sampled adjacent to those craters. One of these craters may have excavated underlying material, which we infer to be Slater ejecta based on ejecta thickness calculations. One large and five small PSRs also occur within the boundaries of the site. Because of the small sizes of these PSRs, they must be young (e.g., Kring 2019) and, thus, any volatiles will be dominated by solar wind products. Most of the PSRs in this site would be accessible to a crew engaged in EVA.

Site 011 is located on what is calculated to be a thin veneer of Shackleton crater ejecta but is dominated by de Gerlache ejecta and potentially a layer of ejecta from Cabeus, which is of intermediate age between the de Gerlache and Shackleton impacts. Large boulder fields on the rim of de Gerlache represent de Gerlache ejecta. A large PSR on the floor of the de Gerlache is much older than the small PSRs within Site 007 and may have trapped volatiles from a variety of sources (impacts, volcanism, solar wind), but would not be accessible to a crew at Site 011 due to the steep crater walls.

Both sites contain locations of geologic and ISRU interest. In general, Site 007 offers more opportunities for ISRU experiments, given the direct detection of water within a PSR located within the 10 km EZ. Site 011 offers a somewhat more diverse geology with ejecta from several large impacts. Site 007 primarily has slopes $<15^{\circ}$, while Site 011 has more dramatic topography and higher slopes (up to and including 15°–25°), especially on crater walls. Both sites offer accessible opportunities to address open questions in lunar science.

We would like to thank the two anonymous reviewers for their detailed comments and suggestions, which helped in improving the manuscript. We thank E. Mazarico, J. Kloos, T. D. Glotch, R. L. Klima, and V. Bickel for clarification of several details regarding polar maps. We thank S. Li for providing data in Li et al. (2018). We thank S. F. A. Cartwright for his development of the Lunar Season Calculator to facilitate this study. We also extend our gratitude to Delia Enriquez for her assistance. This work was supported by NASA Solar System Exploration Research Virtual Institute contract 80NSSC20M0016 (PI: D.A.K.) and RISE2 award number 80NSSC19M0215 (PI: T.D.G.). This is LPI Contribution No. 2842.

Data Availability

NAC Mosaics are available at https://wms.lroc.asu.edu/lroc/view_rdr/NAC_POLE_SOUTH. LOLA illumination data was downloaded from http://imbrium.mit.edu/BROWSE/EXTRAS/ILLUMINATION/. LOLA south pole DEMS were downloaded from http://imbrium.mit.edu/BROWSE/LOLA_GDR/POLAR/SOUTH_POLE/. Hourly temperature maps of the south pole are available at http://luna1.diviner.ucla.edu/~jpierre/diviner/level4_polar/hourly_maps/south/. Fraction below 110 K maps in summers at the south pole were downloaded from http://luna1.diviner.ucla.edu/~jpierre/diviner/level4_polar/additional_maps/. IFI and ITT maps were downloaded from https://kevincannon.rocks/lunarmining/.

Appendix A
Supplementary Figures

Figure A1 displays the illumination in 2024 December at the two sites. Figure A2 displays the Earth visibility from the two sites. Figure A3 displays hillshade images of the two sites. Figure A4 displays the SSRs in the two sites. Figure A5 displays ejecta thickness of de Gerlache over Site 011.

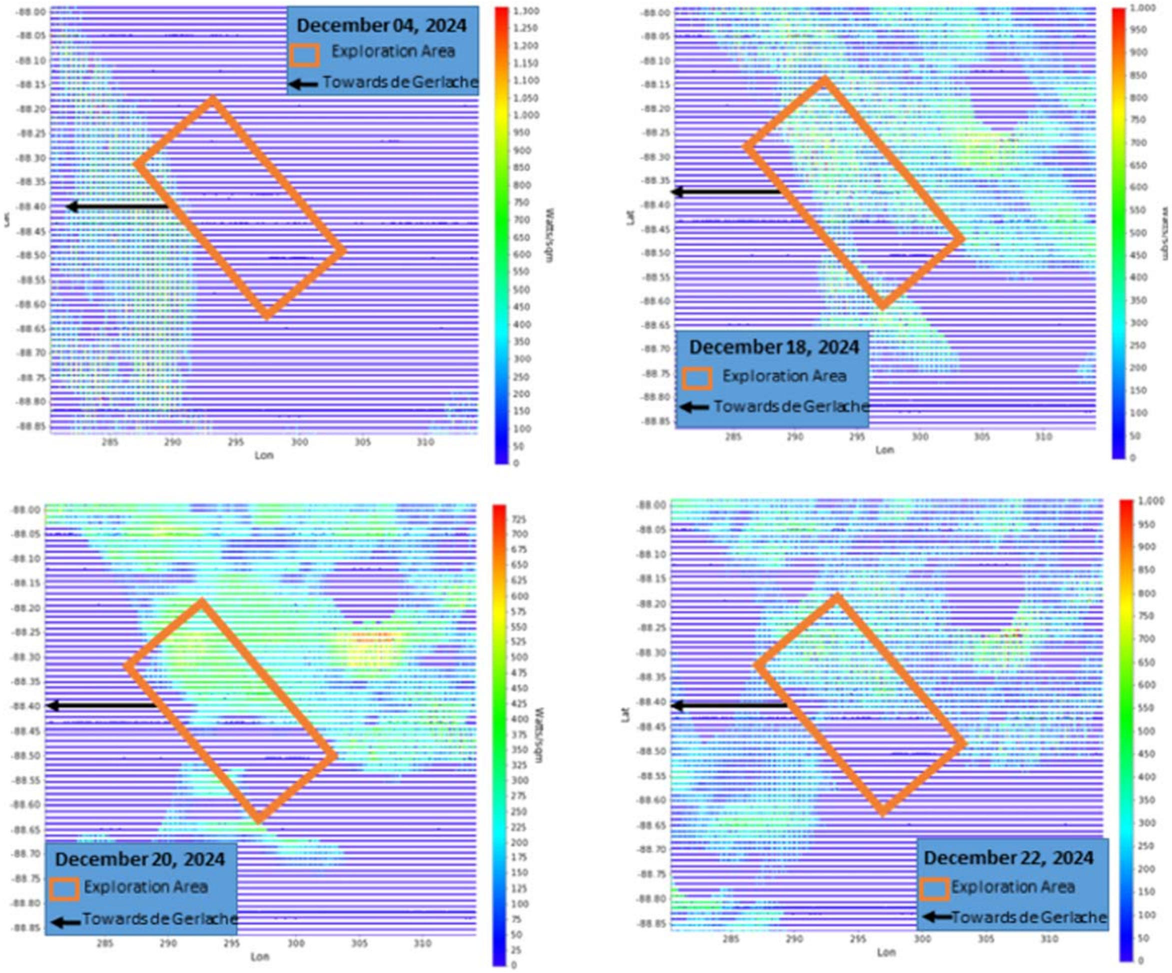

Figure A1. Illumination conditions at Site 011 during 2024 December. Areas along traverses are shown as orange boxes; black arrows point toward the center of de Gerlache. Top-left panel: example of a day for which illumination conditions are somewhat favorable for the western portion of the exploration area. Top-right panel: example of a day for which illumination conditions are favorable for the eastern portion of the exploration area. Bottom-left panel: example of a day for which illumination conditions are favorable for the eastern portion of the exploration area. Bottom-right panel: example of a day for which illumination conditions are favorable for the center/overlapping portion of the exploration area.

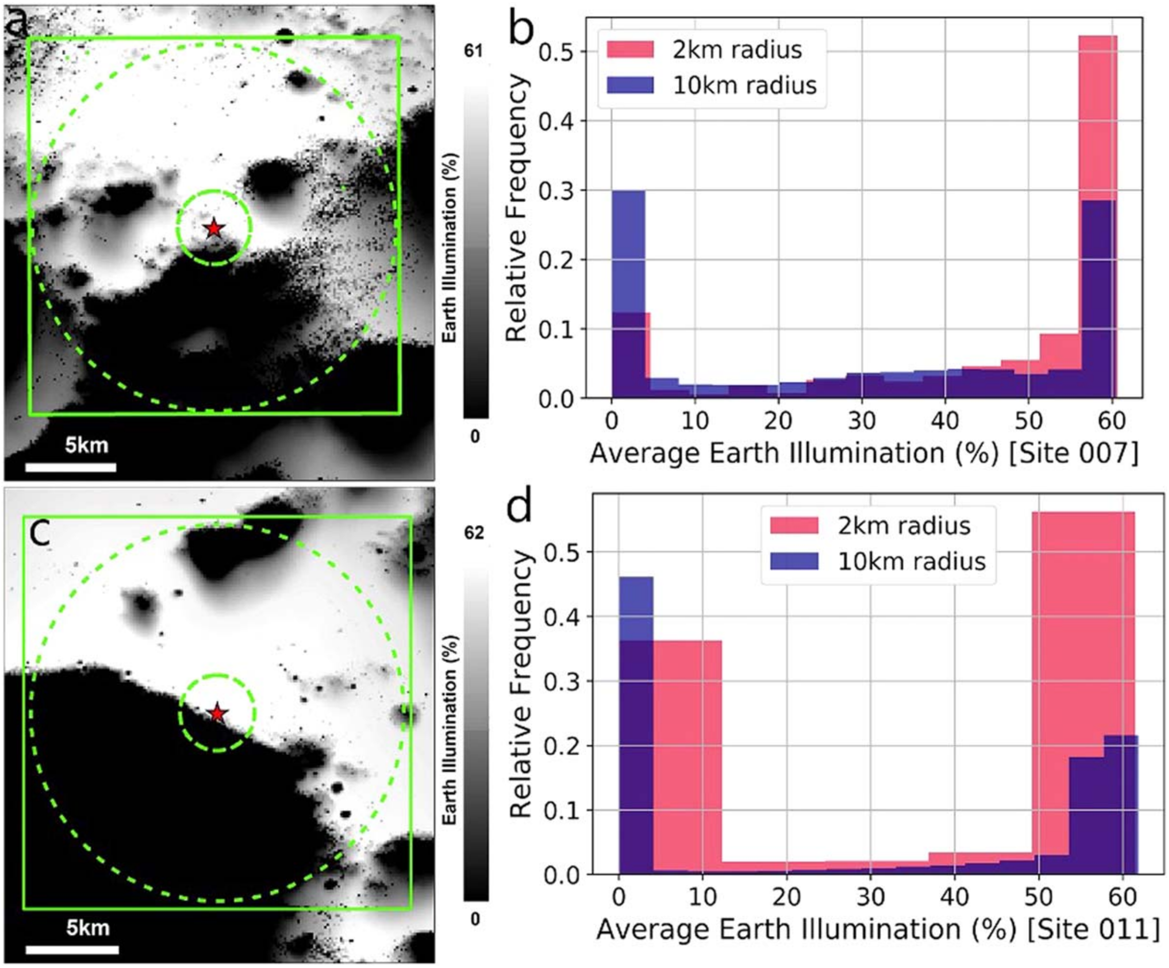

Figure A2. (a) Earth illumination map of Site 007. (b) Locations within the 2 km EZ and within the 10 km EZ in Site 007 from whence the Earth is directly visible over a period. (c) Earth illumination map of Site 011. (d) Locations within the 2 km EZ and within the 10 km EZ in Site 011 from whence the Earth is directly visible over a period.

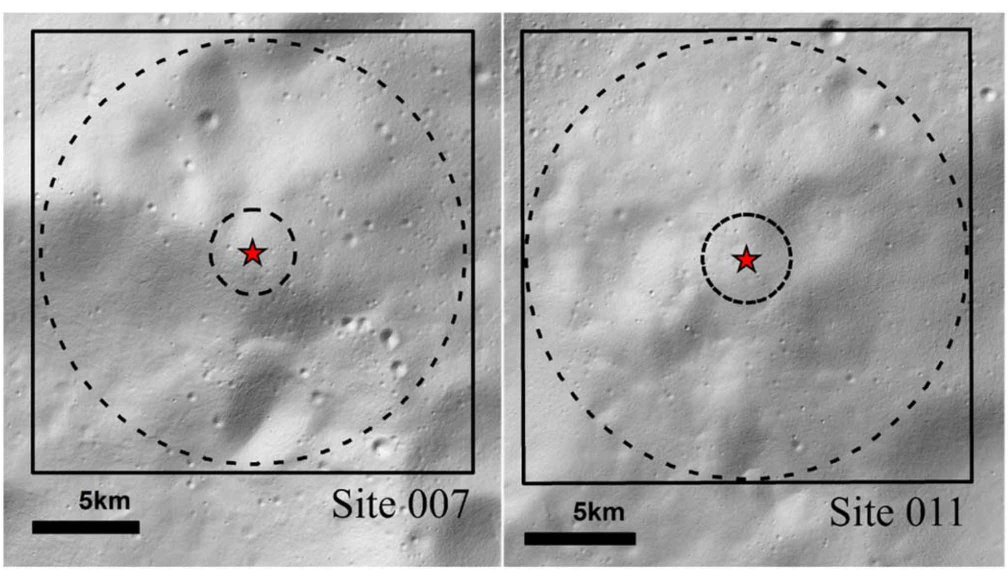

Figure A3. Hillshade image of the two sites derived from a LOLA digital elevation model.

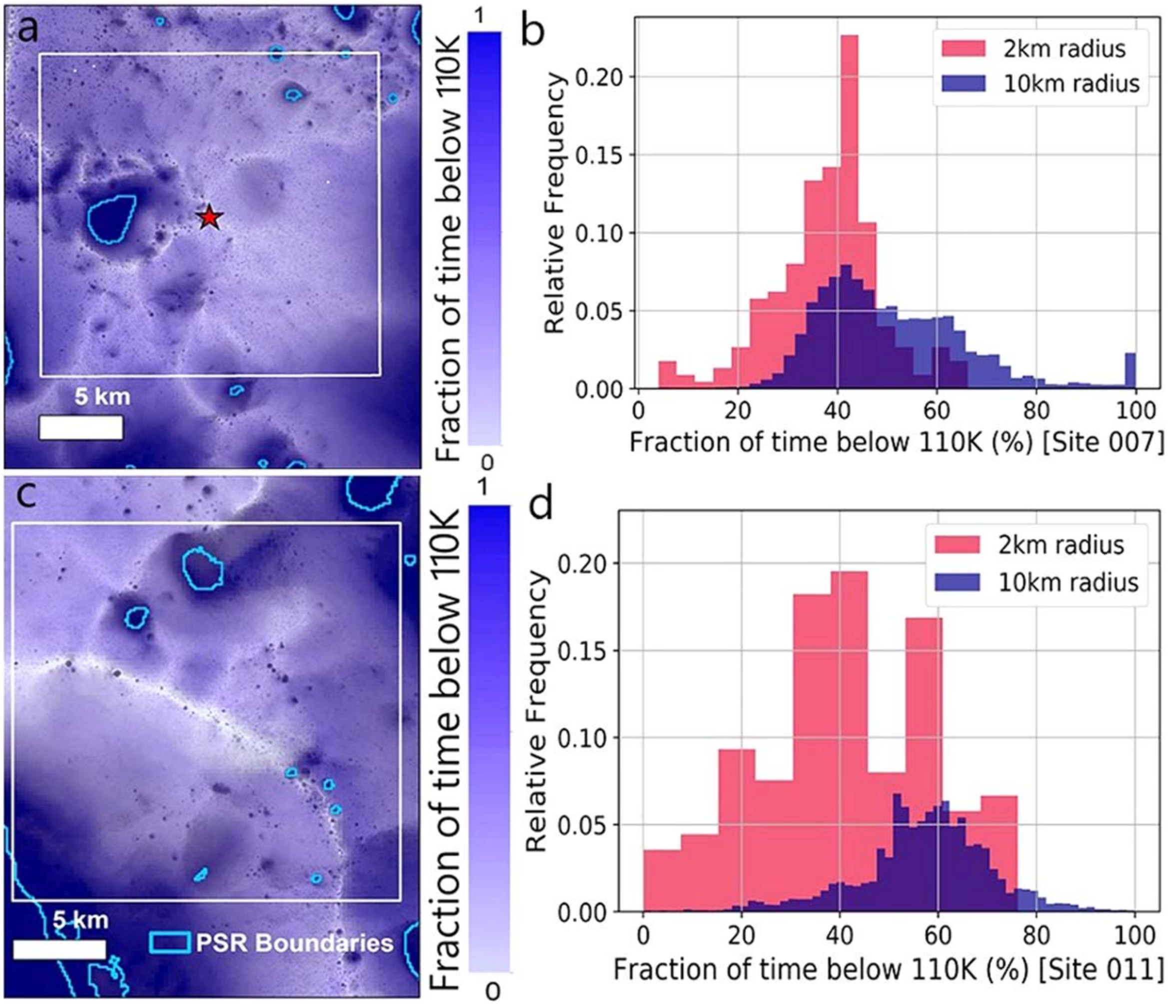

Figure A4. (a) Fraction of time locations within Site 007 remain below 110 K. (b) Locations within the 2 km EZ in Site 007 which remain 110 K over a period of time. (c) Fraction of time locations within Site 011 remain below 110 K. (d) Locations within the 2 km EZ in Site 011 which remain 110 K over a period of time.

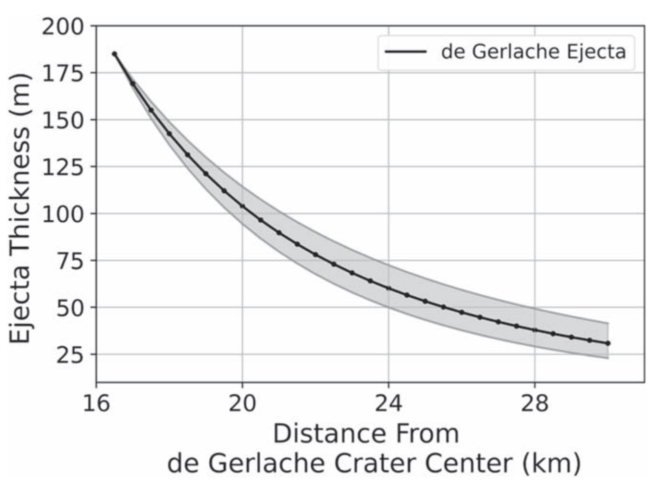

Figure A5. de Gerlache crater ejecta thickness over Site 011.

Appendix B
Supplementary Tables

Tables B1–B4 display ejecta thickness at the two sites from Shackleton, Slater, Cabeus, and de Gerlache. Tables B5 and B6 display excavated crater depths in the two sites.

Table B1
Ejecta Thickness from the Rim of the Shackleton Crater Covering the Two Sites Calculated at an Interval of 500 m As a Function of Scaling Exponents −2.5, −3.0, and −3.5

Distance from Shackleton Center (m)	−2.5 (m)	−3 (m)	−3.5 (m)
12500	271.611 094	248.935 68	228.153 319
13000	246.243 15	221.302 913	198.888 698
13500	224.072 272	197.613 169	174.278 433
14000	204.598 502	177.187 5	153.448 876
14500	187.414 217	159.482 554	135.713 743
15000	172.184 633	144.06	120.529 243
15500	158.632 911	130.563 593	107.461 004
16000	146.528 661	118.701 782	96.159 433 9
16500	135.679 014	108.234 41	86.341 190 5
17000	125.921 6	98.962 446 6	77.775 106 1
17500	117.119 016	90.72	70.271 409 8
18000	109.154 407	83.368 055 6	63.673 404 2
18500	101.927 933	76.789 528 8	57.850 989
19000	95.353 916 5	70.885 333 1	52.695 585 4
19500	89.358 528 7	65.571 233 5	48.116 130 9
20000	83.877 9	60.775 312 5	44.035 897 5
20500	78.856 570 5	56.435 919 4	40.389 950 7
21000	74.246 212	52.5	37.123 106
21500	70.004 569 4	48.921 730 2	34.188 278 1
22000	66.094 578 3	45.661 391 8	31.545 139 6
22500	62.483 628 7	42.684 444 4	29.159 026 7
23000	59.142 945 2	39.960 754 5	27.000 040 2
23500	56.047 066	37.463 953 1	25.042 306 1
24000	53.173 400 4	35.170 898 4	23.263 362 7
24500	50.501 854 6	33.061 224 5	21.643 652
25000	48.014 511 7	31.116 96	20.166 094 9
25500	45.695 358 3	29.322 206 4	18.815 735 8
26000	43.530 050 2	27.662 864 1	17.579 443 4
26500	41.505 710 6	26.126 399 6	16.445 658 9
27000	39.610 755 7	24.701 646 1	15.404 182 8
27500	37.834 744 3	23.378 632 6	14.445 993 3
28000	36.168 247	22.148 437 5	13.563 092 6
28500	34.602 731 9	21.003 061 7	12.748 374 9
29000	33.130 465 9	19.935 319 2	11.995 513 5
29500	31.744 427 4	18.938 742 5	11.298 864
30000	30.438 230 5	18.007 5	10.653 380 7
30500	29.206 057 8	17.136 324 2	10.054 544 5
31000	28.042 601 7	16.320 449 1	9.498 300 57
31500	26.943 012 6	15.555 555 6	8.981 004 19
32000	25.902 852 5	14.837 722 8	8.499 373 47
32500	24.918 054 7	14.163 386 4	8.050 448 46
33000	23.984 887 6	13.529 301 3	7.631 555 16
33500	23.099 922 4	12.932 508 3	7.240 274 18
34000	22.260 004 4	12.370 305 8	6.874 413 12
34500	21.462 227 8	11.840 223 6	6.531 982 38
35000	20.703 912 7	11.34	6.211 173 8
35500	19.982 584 4	10.867 562	5.910 341 86
36000	19.295 955 4	10.421 006 9	5.627 986 99
36500	18.641 908 7	9.998 586 18	5.362 740 86
37000	18.018 483 1	9.598 691 09	5.113 353 33
37500	17.423 859 8	9.219 84	4.878 680 75
38000	16.856 350 2	8.860 666 64	4.657 675 73
38500	16.314 385 3	8.519 909 84	4.449 377 8
39000	15.796 505 4	8.196 404 19	4.252 905 3
39500	15.301 351 8	7.889 071 66	4.067 447 93
40000	14.827 658	7.596 914 06	3.892 260 22
40500	14.374 242 9	7.319 006 25	3.726 655 57
41000	13.940 003 9	7.054 489 92	3.570 001 01
41500	13.523 910 8	6.802 568 09	3.421 712 36
42000	13.125	6.562 5	3.281 25
42500	12.742 37	6.333 596 58	3.148 114 95
43000	12.375 176 4	6.115 216 27	3.021 845 41
43500	12.022 627 6	5.906 761 24	2.902 013 56
44000	11.683 981 1	5.707 673 98	2.788 222 77
44500	11.358 54	5.517 434 1	2.680 104 94
45000	11.045 649 4	5.335 555 56	2.577 318 19
45500	10.744 693 9	5.161 583 98	2.479 544 74
46000	10.455 094 4	4.995 094 31	2.386 488 94
46500	10.176 306	4.835 688 63	2.297 875 54
47000	9.907 815 1	4.682 994 13	2.213 448 05
47500	9.649 137 92	4.536 661 32	2.132 967 33
48000	9.399 818	4.396 362 3	2.056 210 19
48500	9.159 424 59	4.261 789 27	1.982 968 21
49000	8.927 550 96	4.132 653 06	1.913 046 63
49500	8.703 812 78	4.008 681 86	1.846 263 32
50000	8.487 846 7	3.889 62	1.782 447 81
50500	8.279 309 02	3.775 226 85	1.721 440 49
51000	8.077 874 43	3.665 275 8	1.663 091 79
51500	7.883 234 86	3.559 553 3	1.607 261 48
52000	7.695 098 42	3.457 858 02	1.553 817 95
52500	7.513 188 4	3.36	1.502 637 68
53000	7.337 242 35	3.265 799 96	1.453 604 62
53500	7.167 011 2	3.175 088 55	1.406 609 67
54000	7.002 258 49	3.087 705 76	1.361 550 26
54500	6.842 759 6	3.003 500 31	1.318 329 83
55000	6.688 301 07	2.922 329 08	1.276 857 48
55500	6.538 679 95	2.844 056 62	1.237 047 56
56000	6.393 703 18	2.768 554 69	1.198 819 35
56500	6.253 187 03	2.695 701 77	1.162 096 7
57000	6.116 956 6	2.625 382 71	1.126 807 79
57500	5.984 845 26	2.557 488 29	1.092 884 79
58000	5.856 694 28	2.491 914 9	1.060 263 62
58500	5.732 352 29	2.428 564 2	1.028 883 74
59000	5.611 674 97	2.367 342 81	0.998 687 92
59500	5.494 524 62	2.308 162 02	0.969 621 99
60000	5.380 769 8	2.250 937 5	0.941 634 71
60500	5.270 285	2.195 589 09	0.914 677 56
61000	5.162 950 37	2.142 040 52	0.888 704 57
61500	5.058 651 36	2.090 219 24	0.863 672 18
62000	4.957 278 46	2.040 056 14	0.839 539 09
62500	4.858 726 97	1.991 485 44	0.816 266 13
63000	4.762 896 72	1.944 444 44	0.793 816 12
63500	4.669 691 87	1.898 873 4	0.772 153 77

Table B2
Ejecta Thickness from the Rim of the Slater Crater Covering Site 007 Calculated at an Interval of 500 m As a Function of Scaling Exponents −2.5, −3.0, and −3.5

Distance from Slater crater Center (m)	−2.5 (m)	−3 (m)	−3.5 (m)
14000	113.447 881	107.198 171	101.292 751
14500	103.919 362	96.486 705 5	89.585 657
15000	95.474 706 1	87.156 083 7	79.562 255 1
15500	87.960 407 4	78.990 777 7	70.935 812 5
16000	81.248 718 8	71.814 4	63.475 561 5
16500	75.232 694 6	65.481 655 7	56.994 465 6
17000	69.822 303 8	59.872 131 6	51.339 929 3
17500	64.941 356 5	54.885 463 8	46.386 683 2
18000	60.525 058 1	50.437 548 4	42.031 290 4
18500	56.518 048 4	46.457 549 6	38.187 870 5
19000	52.872 820 1	42.885 520 1	34.784 750 1
19500	49.548 435 9	39.670 497 8	31.761 817 9
20000	46.509 480 5	36.768 972 8	29.068 425 3
20500	43.725 202 1	34.143 646 5	26.661 708 6
21000	41.168 803 1	31.762 421 2	24.505 239 9
21500	38.816 853 5	29.597 573 3	22.567 938 1
22000	36.648 801 4	27.625 073 5	20.823 182 6
22500	34.646 564 9	25.824 024 8	19.248 091 6
23000	32.794 188 4	24.176 196 5	17.822 928 5
23500	31.077 553 5	22.665 635 4	16.530 613 5
24000	29.484 133 8	21.278 340 7	15.356 319 7
24500	28.002 787 6	20.001 991 2	14.287 136 6
25000	26.623 580 2	18.825 714 1	13.311 790 1
25500	25.337 632 1	17.739 890 8	12.420 407 9
26000	24.136 989 9	16.735 991 3	11.604 322
26500	23.014 513 2	15.806 432 6	10.855 902 4
27000	21.963 779 1	14.944 458 8	10.168 416 3
27500	20.978 998 1	14.144 037 6	9.535 908 22
28000	20.054 941 5	13.399 771 4	8.953 098 88
28500	19.186 878 6	12.706 820 8	8.415 297 63
29000	18.370 521 4	12.060 838 2	7.918 328 19
29500	17.601 976 5	11.457 910 8	7.458 464 64
30000	16.877 703	10.894 510 5	7.032 376 26
30500	16.194 475 2	10.367 450 4	6.637 080 01
31000	15.549 350 1	9.873 847 22	6.269 899 25
31500	14.939 638 7	9.411 087 75	5.928 428 04
32000	14.362 88	8.976 8	5.610 5
32500	13.816 819 2	8.568 827 53	5.314 161 24
33000	13.299 387 1	8.185 206 96	5.037 646 64
33500	12.808 682 5	7.824 148 11	4.779 359 14
34000	12.342 956 1	7.484 016 45	4.537 851 52
34500	11.900 596 8	7.163 317 47	4.311 810 42
35000	11.480 118 4	6.860 682 97	4.100 042 28
35500	11.080 148 9	6.574 858 72	3.901 460 87
36000	10.699 419 8	6.304 693 55	3.715 076 3

Table B3
Ejecta Thickness of the Cabeus Crater Covering Site 011 Calculated at an Interval of 500 m As a Function of Scaling Exponents −2.5, −3.0, and −3.5

Distance from Cabeus Crater Center (m)	−2.5 (m)	−3 (m)	−3.5 (m)
93000	91.956 986 2	67.762 425 7	49.933 632 3
93500	90.732 541	66.681 131	49.005 276 2
94000	89.530 800 3	65.622 720 2	48.098 993 8
94500	88.351 225 8	64.586 591 3	47.214 147 1
95000	87.193 294 6	63.572 160 9	46.350 119 7
95500	86.056 498 6	62.578 864	45.506 316
96000	84.940 344 5	61.606 153 1	44.682 160 4
96500	83.844 352 9	60.653 497 6	43.877 096 6
97000	82.768 057 9	59.720 383 4	43.090 586 9
97500	81.711 006 8	58.806 311 9	42.322 111 2
98000	80.672 759 3	57.910 799 8	41.571 166 8
98500	79.652 887 6	57.033 378 4	40.837 267 2
99000	78.650 975 6	56.173 593 4	40.119 942 1
99500	77.666 618 8	55.331 003 6	39.418 736 2
100000	76.699 423 7	54.505 181 5	38.733 209
100500	75.749 007 4	53.695 711 9	38.062 934 1
101000	74.814 997 6	52.902 192 1	37.407 498 8
101500	73.897 031 9	52.124 231 3	36.766 503 6
102000	72.994 757 7	51.361 449 8	36.139 561 4
102500	72.107 831 8	50.613 479 4	35.526 297 6
103000	71.235 920 2	49.879 962 2	34.926 349 2
103500	70.378 697 7	49.160 550 8	34.339 364 6
104000	69.535 847 6	48.454 907 8	33.765 002 9
104500	68.707 061 5	47.762 705 4	33.202 934
105000	67.892 039 2	47.083 625 1	32.652 837 9
105500	67.090 488 1	46.417 357 3	32.114 404 3
106000	66.302 123 4	45.763 601 4	31.587 332 4
106500	65.526 667 5	45.122 065	31.071 330 6
107000	64.763 849 8	44.492 463 9	30.566 116
107500	64.013 406 7	43.874 521 9	30.071 414 3
108000	63.275 081 3	43.267 970 3	29.586 959 3
108500	62.548 623 3	42.672 548	29.112 492 9
109000	61.833 788 5	42.088 000 7	28.647 764 4
109500	61.130 338 8	41.514 081 4	28.192 530 7
110000	60.438 042 2	40.950 549 6	27.746 555 8
110500	59.756 672 4	40.397 171 3	27.309 610 5
111000	59.086 008 7	39.853 718 9	26.881 472 4
111500	58.425 835 6	39.319 970 9	26.461 925 5
112000	57.775 943 2	38.795 711 6	26.050 760 1
112500	57.136 126 5	38.280 731	25.647 772 4
113000	56.506 185 7	37.774 824 9	25.252 764 4
113500	55.885 925 4	37.277 794 1	24.865 543 9
114000	55.275 155 4	36.789 445	24.485 924 1
114500	54.673 689 8	36.309 588 7	24.113 723 4
115000	54.081 347	35.838 041 6	23.748 765 4
115500	53.497 95	35.374 624 4	23.390 878 6
116000	52.923 325 7	34.919 162 7	23.039 896 1
116500	52.357 305 4	34.471 486 7	22.695 656
117000	51.799 724 1	34.031 430 5	22.358 000 6
117500	51.250 420 6	33.598 832 8	22.026 776 5
118000	50.709 237 8	33.173 536 2	21.701 834 8
118500	50.176 021 7	32.755 387 3	21.383 030 4
119000	49.650 622 4	32.344 236 6	21.070 222 1
119500	49.132 893 1	31.939 938 4	20.763 272 8
120000	48.622 690 4	31.542 350 4	20.462 048 9
120500	48.119 874 2	31.151 334	20.166 420 3
121000	47.624 307 6	30.766 754	19.876 260 6

Table B4
Ejecta Thickness of the de Gerlache Crater Covering Site 011 Calculated at an Interval of 500 m As a Function of Scaling Exponents −2.5, −3.0, and −3.5

Distance from de Gerlache Center (m)	−2.5 (m)	−3 (m)	−3.5 (m)
16500	184.955 033	184.955 033	184.955 033
17000	171.653 914	169.110 753	166.605 27
17500	159.654 4	155.025 75	150.531 292
18000	148.797 198	142.462 471	136.397 431
18500	138.946 206	131.220 836	123.924 995
19000	129.984 633	121.131 525	112.881 392
19500	121.811 835	112.050 591	103.071 553
20000	114.340 747	103.855 141	94.331 116 4
20500	107.495 767	96.439 822 8	86.520 983 1
21000	101.211 015	89.713 975 7	79.522 94
21500	95.428 888 4	83.599 293 5	73.236 123 7
22000	90.098 863 5	78.027 904 6	67.574 147 6
22500	85.176 486 1	72.940 785	62.462 756 5
23000	80.622 530 4	68.286 441 1	57.837 902 3
23500	76.402 287 1	64.019 812 8	53.644 159
24000	72.484 961 2	60.101 354 8	49.833 410 8
24500	68.843 161 1	56.496 264 6	46.363 761 6
25000	65.452 462 9	53.173 832 2	43.198 625 5
25500	62.291 037 4	50.106 889 7	40.305 965 4
26000	59.339 330 9	47.271 343 2	37.657 652 3
26500	56.579 789 9	44.645 774 9	35.228 925 8
27000	53.996 623 6	42.211 102 4	32.997 936 7
27500	51.575 599	39.950 287 2	30.945 359 4
28000	49.303 861 7	37.848 083 5	29.054 061 4
28500	47.169 781 5	35.890 822 2	27.308 820 9
29000	45.162 816 7	34.066 223 7	25.696 085 4
29500	43.273 395 6	32.363 235 9	24.203 763 6
30000	41.492 812 9	30.771 893 7	22.821 047 1

Table B5
Location, Diameter, Depth, and Distance from the Shackleton and Slater Crater Rims, and Depth Excavated by 30 Craters in Site 007

Latitude	Longitude	Diameter (m)	Depth (m)	Distance from Shackleton Rim (km)	Distance from Slater Rim (km)	Excavated Depth (m)
−89.2439	120.445 3	621	70	2.5	23.5	151.302 9
−89.1725	124.774 5	410	80	4.25	22	71.509 94
−89.1782	114.063 3	346	50	5	21	80.563 59
−89.1666	117.263 9	364	30	5	20.75	100.563 6
−89.1468	121.505 4	96	15	5	20.5	115.563 6
−89.1189	131.137 2	206	35	6	21.8	73.234 41
−89.1352	116.515 6	190	30	6	19.75	78.234 41
−89.1336	113.957 0	258	35	6	19.5	73.234 41
−89.1439	112.145 0	247	30	6	19.9	78.234 41
−89.0924	122.402 5	211	20	7.1	19.1	70.72
−89.0972	118.962 4	208	50	7	18.9	40.72
−89.0264	122.983 2	48	5	9	17.4	60.571 23
−89.0191	116.579 0	56	10	9.4	16.4	51.696 14
−88.9402	120.414 3	122	15	11.7	14.6	29.438 39
−88.9044	136.881 3	146	25	12.75	19.1	13.685 51
−88.8920	129.918 5	290	60	13	16	−22.536
−88.6740	109.607 7	112	20	20.4	15.7	−3.52059
−88.6253	109.311 4	88	10	21.9	14.25	4.294 934
−88.8675	109.931 4	132	15	14.5	11.5	16.116 96
−88.8081	111.338 5	110	10	16.2	9.7	15.543 68
−88.8442	116.743 4	96	10	12.8	11.1	28.437
−88.6696	118.794 4	122	30	19.9	6.5	−12.694
−88.8197	130.260 2	281	60	15.2	14.5	−31.357
−88.8067	132.916 0	142	20	15.6	15.5	7.346 117
−88.7141	133.153 8	58	7	18.5	14.4	12.935 32
−88.6194	132.432 5	121	10	21.3	11.8	5.119 444
−88.8756	126.101 6	143	20	13.7	14.1	14.306 08
−88.8343	123.869 9	94	10	15	12.3	19.322 21
−88.7343	123.378 9	86	15	17.8	9.8	6.451 511
−88.7401	119.636 6	40	10	17.75	8.75	11.565 61

Table B6
Location, Diameter, Depth, and Distance from the Shackleton, Cabeus and de Gerlache Crater Rims, and Depth Excavated by 30 Craters in Site 011

Latitude	Longitude	Diameter (m)	Depth (m)	Distance from Shackleton rim (km)	Distance from Cabeus rim (km)	Distance from de Gerlache rim (km)	Excavated Depth (m)
−88.9503	−79.6705	1074	320	30.5	67.5	0	−279.772
−88.8633	−81.8280	496	140	33	66.75	0	−100.92
−88.9498	−74.6837	277	40	30.75	65.5	0.5	1.846 165
−88.8361	−76.5483	515	150	34	63.75	0	−107.934
−88.7606	−79.4510	3892	930	36	63.5	0	−888.375
−88.6236	−82.2233	411	80	40	62.5	0	−38.4499
−88.6437	−78.4740	435	100	39.75	60.75	0	−56.5825
−88.5238	−75.2432	85	18	43.5	56.5	0	29.580 17
−88.6618	−68.3806	127	16	39.75	56.25	0	32.637 64
−88.4982	−67.8828	453	60	44.75	52	0	−6.50368
−88.3760	−68.8424	230	50	48.35	49.62	0	6.694 924
−88.3253	−69.5564	333	90	49.87	48.87	0	−32.2418
−88.3836	−65.3403	94	12	48.3	48	2.65	47.424 96
−88.3987	−63.0564	27	4	47.945	47.4	4.35	56.523 87
−88.3999	−63.1807	35	10	47.9	47.5	4.335	50.351 86
−88.4609	−61.9867	364	50	46	48.5	4.75	8.869 295
−88.5255	−64.6143	646	120	44	51.25	2.25	−65.2555
−88.5211	−61.7207	871	280	44.25	50	4.5	−93.3417
−88.5457	−56.1949	329	60	43.7	49	8.5	−1.61535
−88.6082	−57.9099	462	50	41.75	51.25	7	5.149 427
−88.6394	−64.3713	137	20	40.6	54.2	2.2	31.133 32
−88.7592	−57.5054	110	20	37.1	55.4	7.1	30.401 5
−88.7824	−55.7622	108	20	36.5	55.6	8.3	30.317 32
−88.8218	−61.9982	111	30	35.2	58.26	4.6	17.461 36
−88.8442	−59.4639	48	6	34.5	58.25	6.25	41.714 49
−88.8714	−70.0294	678	100	33.5	62	0.75	−56.0116
−88.9172	−70.4237	1003	190	32	63.5	1.5	−146.877
−88.9450	−72.6225	873	140	31	65	1	−97.8228
−88.9897	−73.3050	273	40	29.5	66	1.72	2.068 401
−88.9412	−62.6574	96	20	31.5	61.7	5.5	25.151 12

ORCID iDs

Nandita Kumari https://orcid.org/0000-0001-5960-0914
Jordan M. Bretzfelder https://orcid.org/0000-0002-7341-5675
Indujaa Ganesh https://orcid.org/0000-0002-1317-3563

References

Allender, E. J., Orgel, C., Almeida, N. V., et al. 2019, ASR, 63, 692
Arnold, J. 1976, in Lunar Science Inst., Abstracts of Papers Presented at a Special Session of the Seventh Annual Lunar Science Conference on Utilization of Lunar Materials and Expertise for Large Scale Operations in Space (Houston, TX: Lunar Science Inst.), https://ntrs.nasa.gov/citations/19910073649
Arnold, J. R. 1979, JGR, 84, 5659
Arvidson, R., Crozaz, G., Drozd, R. J., Hohenberg, C. M., & Morgan, C. J. 1975, Moon, 13, 259
Bailen, M. S., Sucharski, R. M., Akins, S. W., et al. 2013, LPSC, 44, 2246
Barker, M. K., Mazarico, E., Neumann, G. A., et al. 2021, P&SS, 203, 105119
Basilevsky, A. T., Head, J. W., Horz, F., & Ramsley, K. 2015, P&SS, 117, 312
Benna, M., Hurley, D. M., Stubbs, T. J., et al. 2019, NatGeo, 12, 333
Borst, A. M., Foing, B. H., Davies, G. R., & Van Westrenen, W. 2012, P&SS, 68, 76
Blalock, J. J, Mayer, D. P, Lemelin, M., et al. 2020, LPI Contribution, 2241, 5112
Bussey, D. Ben J., Spudis, P. D., & Robinson, M. S. 1999, GeoRL, 26, 1187
Bussey, D. B. J., Lucey, P. G., Steutel, D., et al. 2003, GeoRL, 30, 1278
Bussey, D. B. J., Fristad, K. E., Schenk, P. M., Robinson, M. S., & Spudis, P. D. 2005, Natur, 434, 842
Bussey, D. B. J., McGovern, J. A., Spudis, P. D., et al. 2010, Icar, 208, 558
Campbell, D. B., Campbell, B. A., Carter, L. M., Margot, J.-L., & Stacy, N. J. S. 2006, Natur, 443, 835
Cannon, K. M., & Britt, D. T. 2020, Icar, 347, 113778
Cartwright, S. F. A., & Bretzfelder, J. M. 2021, LPSC, 52, 2533
Colaprete, A., Schultz, P., Heldmann, J., et al. 2010, Sci, 330, 463
Crider, D. H., & Vondrak, R. R. 2000, JGR, 105, 26773
Crider, D. H., & Vondrak, R. R. 2003, JGRE, 108, 5079
De Rosa, D., Bussey, B., Cahill, J. T., et al. 2012, P&SS, 74, 224
Day, B., & Law, E. 2018, COSPAR Scientific Assembly, 42, B3.1–11–18
Deutsch, A. N., Head, J. W., & Neumann, G. A. 2020, Icar, 336, 113455
Elphic, R. C., Eke, V. R., Teodoro, L. F. A., Lawrence, D. J., & Bussey, D. B. J. 2007, GeoRL, 34, L13204
Fassett, C. I., & Minton, D. A. 2013, NatGeo, 6, 520
Feldman, W. C., Maurice, S., Binder, A. B., et al. 1998, Sci, 281, 1496
Flahaut, J., Carpenter, J., Williams, J. P., et al. 2020, P&SS, 180, 104750
Gault, D. E., Hörz, F., & Hartung, J. B. 1972, LPSC, 3, 2713
Gawronska, A. J., Barrett, N., Boazman, S. J., et al. 2020, AdSpR, 66, 1247
Gladstone, G. R., Retherford, K. D., Egan, A. F., et al. 2012, JGRE, 117, E00H04
Glaser, P., Scholten, F., De Rosa, D., et al. 2014, Icar, 243, 78
Halim, S. H., Barrett, N., Boazman, S. J., et al. 2021, Icar, 354, 113992
Hartmann, W. K. 1969, Icar, 10, 201
Haruyama, J., Ohtake, M., Matsunaga, T., et al. 2008, Sci, 322, 938
Haruyama, J., Yamamoto, S., Yokota, Y., Ohtake, M., & Matsunaga, T. 2013, GRL, 40, 3814
Hayne, P. O., Aharonson, O., & Schörghofer, N. 2021, NatAs, 5, 169
Heldmann, J. L., Lamb, J., Asturias, D., et al. 2015, Icar, 254, 262
Hörz, F., Schneider, E., Gault, D. E., Hartung, J. B., & Brownlee, D. E. 1975, The Moon, 13, 235
Hurley, D. M., Lawrence, D. J., Bussey, D. B. J., et al. 2012, GeoRL, 39, L09203
Hurwitz, D., & Kring, D. A. 2015, E&PSL, 427, 31

Ingersoll, A. P., Svitek, T., & Murray, B. C. 1992, Icar, 100, 40
Kato, M., Sasaki, S., Tanaka, K., Iijima, Y., & Takizawa, Y. 2008, AdSpR, 42, 294
Kloos, J. L., Moores, J. E., Sangha, J., et al. 2019, JGRE, 124, 1935
Kramer, G. Y., Kring, D. A., Nahm, A. L., & Pieters, C. M. 2013, Icar, 223, 131
Kring, D. A. 1995, JGR, 100, 16979
Kring, D. A., Kramer, G. Y., Bussey, D. B. J., & Hurley, D. M. 2014, LPI Contribution, 1820, 3057
Kring, D. A. 2019, Lunar South Pole Geology: Preparing for a Seventh Lunar Landing. NASA Exploration Science Forum 2019 (Moffett Field, CA: Ames Research Center), 127, https://www.lpi.usra.edu/exploration/publications/Kring_SSERVI%20ESF2019_SouthPoleGeology.pdf
Kring, D. A., Siegler, M. A., & Paige, D. A. 2020a, LPSC, 51, 1933
Kring, D. A., Siegler, M. A., & Paige, D. A. 2020b, NESF, 1
Kring, D. A., Barrett, N., Boazman, S., et al. 2020c, Artemis III Science Definition Team White Paper, 2040
Kring, D. A., Barrett, N., Boazman, S., et al. 2020d, Artemis III Science Definition Team White Paper, 2042
Kring, D. A., Bretzfelder, J. M., Ganesh, I., et al. 2020e, Artemis III Science Definition Team White Paper, 2043
Kring, D. A., Bretzfelder, J. M., Ganesh, I., et al. 2020f, Artemis III Science Definition Team White Paper, 2044
Kring, D. A., Bretzfelder, J. M., Ganesh, I., et al. 2020g, Artemis III Science Definition Team White Paper, 2045
Kring, D. A., Bretzfelder, J. M., Ganesh, I., et al. 2020h, Artemis III Science Definition Team White Paper, 2047
Kumar, S. P., Sruthi, U., Krishna, N., et al. 2016, JGRE, 121, 147
Kring, D. A., Kramer, G. Y., Bussey, D. B. J., et al. 2021, AdSpR, 68, 4691
Lawrence, D. J., Miller, R. S., Ozimek, M. T., Peplowski, P. N., & Scott, C. J. 2015, ActaAstro, 115, 452
Lawrence, D. J. 2017, JGRE, 122, 21
Lemelin, M., Blair, D. M., Roberts, C. E., et al. 2014, P&SS, 101, 149
Lemelin, M., Li, S., Mazarico, E., et al. 2021, PSJ, 2, 103
Li, S., Lucey, P. G., Milliken, R. E., et al. 2018, PNAS, 115, 8907
Lucey, P. G. 2009, Elements, 5, 41
Lucey, P. G., Neumann, G. A., Riner, M. A., et al. 2014, JGRE, 119, 1665
Lunar Exploration Science Working Group (LExWG) 1995, Lunar Surface Exploration Strategy, Final Rep., https://www.lpi.usra.edu/lunar/strategies/LExSWG.pdf
Mazarico, E., Neumann, G. A., Smith, D. E., et al. 2011, Icar, 21, 1066
Miller, R. S., Lawrence, D. J., & Hurley, D. M. 2014, Icar, 233, 229
Morbidelli, A., Marchi, S., Bottke, W. F., & Kring, D. A. 2012, E&PSL, 355, 144
Morgan, T. H., & Shemansky, D. E. 1991, JGR, 96, 1351
Moriarty, D. P., III, & Pieters, C. M. 2018, JGRE, 123, 729
NASA 2019, White Paper: Initial Evaluation of Mission Design Sensitivity to Surface Stay Duration, https://imlive.s3.amazonaws.com/Federal%20Government/ID27672541098085344880852119640648037009/Attachment_A14_Surface_Mission_Duration_Sensitivity_White_Paper_082819.pdf
NASA 2020, Plan for Sustainable Lunar Exploration and Development, https://www.nasa.gov/sites/default/files/atoms/files/a_sustained_lunar_presence_nspc_report4220final.pdf
NASA 2022, NASA Announcement, August 19, https://www.nasa.gov/press-release/nasa-identifies-candidate-regions-for-landing-next-americans-on-moon
National Research Council of the National Academies 2007, The Scientific Context for Exploration of the Moon, Final Report (Washington, D. C: The National Academies Press), https://doi.org/10.17226/11954
Needham, D. H., & Kring, D. A. 2017, E&PSL, 478, 175
Noda, H., Araki, H., Goossens, S., et al. 2008, GeoRL, 35, L24203
Nozette, S., Spudis, P. D., Robinson, M. S., et al. 2001, JGR, 106, 23253
Öhman, T., & Kring, D. A. 2012, JGRE, 117, E00H08
Ohtake, M., Matsunaga, T., Haruyama, J., et al. 2009, Natur, 461, 236
Paige, D. A., Siegler, M. A., Zhang, J. A., et al. 2010, Sci, 330, 479
Potter, R. W. K., Collins, G. S., Kiefer, W. S., McGovern, P. J., & Kring, D. A. 2012, Icar, 220, 730
Prem, P., Artemieva, N. A., Goldstein, D. B., Varghese, P. L., & Trafton, L. M. 2015, Icar, 255, 148
Robinson, M. S., Brylow, S. M., Tschimmel, M., et al. 2010, SSRv, 150, 81
Schorghofer, N., & Taylor, G. J. 2007, JGRE, 112, E02010
Schultz, P. H., Hermalyn, B., Colaprete, A., et al. 2010, Sci, 330, 468
Siegler, M. A., Bills, B. G., & Paige, D. A. 2011, JGRE, 116, E03010
Siegler, M. A., Miller, R. S., Keane, J. T., et al. 2016, Natur, 531, 480
Smith, D. E., Zuber, M. T., Neumann, G. A., et al. 2010, GeoRL, 37, L18204
Smith, D. E., Zuber, M. T., Neumann, G. A., et al. 2017, Icar, 283, 70
Speyerer, E. J., & Robinson, M. S. 2013, Icar, 222, 122
Speyerer, E. J., Lawrence, S. J., Stopar, J. D., et al. 2016, Icar, 273, 337
Spudis, P. D., Gillis, J. J., & Reisse, R. A. 1994, Sci, 266, 1848
Spudis, P. D., Bussey, B., Plescia, J., Josset, J.-L., & Beauvivre, S. 2008, GRL, 35, 14
Stewart, B. D., Pierazzo, E., Goldstein, D. B., Varghese, P. L., & Trafton, L. M. 2011, Icar, 215, 1
Taylor, G. J., Kring, D. A., & Needham, D. H. 2018, LPI Contribution, 2087, 5007
Thomson, B. J., Bussey, D. B. J., Neish, C. D., et al. 2012, GRL, 39, 14
Teodoro, L. F. A., Eke, V. R., & Elphic, R. C. 2010, GRL, 37, 12
Tye, A. R., Fassett, C. I., Head, J. W., et al. 2015, Icar, 255, 70
USGS Astrogeology Science Center, Wilhelms, D. E., MacCauley, J. F., et al. 2013, Map I-1162, https://astrogeology.usgs.gov/search/map/Moon/Geology/Lunar_Geologic_GIS_Renovation_March2013
Vaughan, W. M., & Head, J. W. 2014, P&SS, 91, 101
Watson, K., Murray, B. C., & Brown, H. 1961, JGR, 66, 3033
Watkins, R. N., Jolliff, B. L., Mistick, K., et al. 2019, JGRE, 124, 2754
Williams, J. P., Greenhagen, B. T., Paige, D. A., et al. 2019, JGRE, 124, 2505
Wood, J. A., Dickey, J. S., Jr., Marvin, U. B., & Powell, B. N. 1970, GeCAS, 1, 965
Yamamoto, S., Nakamura, R., Matsunaga, T., et al. 2012, GeoRL, 39, L13201
Zuber, M. T., Head, J. W., Smith, D. E., et al. 2012, Natur, 486, 378